J. Fluid Mech. (1987), *vol.* 185, *pp.* 67–106
Printed in Great Britain

Swirling recirculating flow in a liquid-metal column generated by a rotating magnetic field

By P. A. DAVIDSON AND J. C. R. HUNT
Department of Applied Mathematics and Theoretical Physics, University of Cambridge, Silver Street, Cambridge CB3 9EW, UK

(Received 25 June 1986 and in revised form 12 May 1987)

In this paper we consider theoretical and experimental aspects of axisymmetric, swirling flow which is generated in a column of liquid metal by a rotating magnetic field. Two cases are discussed, one in which there is no axial variation in the stirring force, and one where the body force is restricted to a relatively short length of the column. The latter case is of considerable practical interest in continuous casting.

One-dimensional stirring, where the swirl is independent of z and θ, is well understood. The magnetic body force is balanced by shear, all inertial forces being zero (except for the centripetal acceleration). However, in two-dimensional axisymmetric stirring, the axial variation in swirl drives a strong secondary poloidal flow. The principal local force balance is between the magnetic torque and inertia. The body force spins up the fluid as it passes through the forced region and the secondary flow sweeps this angular momentum into the unforced region. Consequently, the size and distribution of the swirl is controlled by the secondary flow.

The role of wall friction is considered and shown to control the length of the recirculating eddy. An approximate solution of the inviscid equations of motion, based on the angular momentum integral, is derived for the flow in the forced region. This is compared with the results of numerical experiments.

The analysis predicts that the swirl velocity scales on $\{B(\sigma/\rho\omega)^{\frac{1}{2}}\}\omega R$, has a maximum at the bottom of the driven region, and penetrates an axial distance of the order $\mathbb{R}R$ away from the forced region. (For turbulent flow the Reynolds number $\mathbb{R}$ must be based on an effective eddy viscosity.) All these features were reproduced experimentally.

1. Introduction

Swirling, recirculating flows have generally been studied in truncated cylinders where the flow is driven by the rotation of one or both ends of the cylinder (see Batchelor 1951; Greenspan 1968). The origin of the secondary flow is a radial force imbalance between the centripetal acceleration and radial pressure gradient in the boundary layer on the endwalls of the container. In these boundary layers the swirl velocity adjusts from that of the core of the flow to that of the endwall. Thus the centripetal acceleration changes across the boundary layer. The radial pressure gradient, however, is impressed on the boundary layer by the outer core flow and is such as to balance the centripetal acceleration in the core. The resulting force imbalance within the boundary layer produces radial outflow or inflow, depending on whether the endwall is spinning faster or more slowly than the core. Our study of the

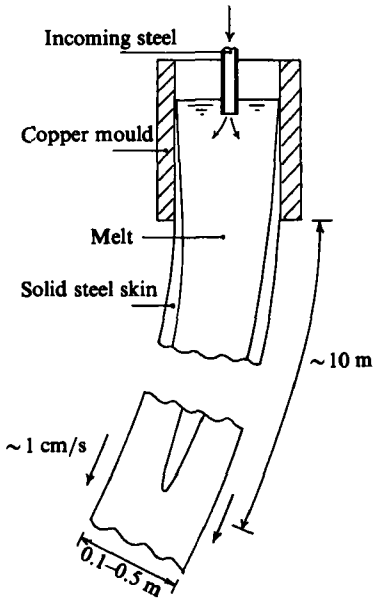

FIGURE 1. Diagrammatic representation of the continuous casting process.

literature indicates that, even for laminar flow, the overall structures of these flows are not well understood.

A different kind of secondary flow can be produced when the swirl is generated by body forces. In this case the swirl may vary axially by virtue of an axial gradient in the body force. Provided this axial gradient is small, the centripetal acceleration is balanced by a radial pressure gradient. The result is an axial variation in pressure which drives a secondary flow. It is this second situation which is discussed here.

The aim of this paper is to show, by detailed calculation and experiment, that some general scaling arguments may be derived. Some of the major qualitative questions that we have considered in our analysis, and that have not been considered in previous studies, are:

(i) How does the flow depend on the variation of the driving force F_θ along the cylinder, or the ratio of its length scale L_f to the radius R?

(ii) What is the effect of wall roughness and the location of the endwalls of the cylinder on the recirculation?

(iii) What is the relative strength of the recirculating flow to the swirling flow?

(iv) Where is the position of maximum swirl? (We shall see that it does not occur at the position of maximum body force.)

This study has been directed particularly towards understanding the swirl generated in a liquid-metal column by the application of an electromagnetic body force. This has the simplifying property that the forcing is independent of the fluid motion (provided that the fluid velocity is not too large), which is not the case for mechanically-driven flows. This magnetohydrodynamic problem has received considerable attention because it is a good representation of rotary electromagnetic stirring of continuously cast steel.

The continuous casting process is shown in figure 1. Molten steel is poured into a water-cooled copper mould where it forms a solid skin. A partially solidified steel strand is slowly drawn from the bottom of the mould. An improved crystalline

structure may be obtained by stirring the steel as it solidifies, and this has led to the increasing use of electromagnetic stirring. Stirrers have been placed at a variety of axial positions along the strand, including around the mould. Despite extensive empirical research, there is, as yet, little consensus as to optimum stirring configurations (Davidson 1986), reflecting a basic lack of understanding of the process. Typical magnetic force distributions are shown in figure 2. This also shows the coordinate system used here.

In this paper we shall restrict attention to axisymmetric flow in a circular column. Often rotation rates are sufficiently low that the free surface of the fluid remains relatively flat and acts as a plane of symmetry. The problems of mould and sub-mould stirring are then identical. We shall ignore the taper, shown in figure 1, which results from the variable shell thickness.

The characteristic velocity and lengthscales can be derived by considering orders of magnitude of terms in the governing equations. This is done in more detail later. However it is instructive to show here that the primary and secondary flows will, in general, be of similar magnitudes.

Independent scales are R, F_θ and L_f the lengthscale along the cylinder of the force. From the Navier–Stokes equations we find that, in the forced region of the flow,

$$\rho u_z \frac{\partial u_\theta}{\partial z} \sim F_\theta,$$

$$\frac{\rho u_\theta^2}{r} \sim \frac{\partial p}{\partial r},$$

$$\rho u_z \frac{\partial u_z}{\partial z} \sim \frac{\partial p}{\partial z},$$

and hence,

$$u_\theta \sim u_z \sim (F_\theta L_f/\rho)^{\frac{1}{2}}.$$

We have assumed here that the body force is balanced by inertia, rather than shear. This will be true provided there exists a sizeable secondary flow. This, in turn, requires F_θ to vary significantly with z. Note that the primary and secondary flows are of the same order of magnitude.

When F_θ does not vary significantly with z (i.e. $L_f \to \infty$), we get a one-dimensional swirl flow, $\boldsymbol{u} = u_\theta(r)\,\hat{\boldsymbol{e}}_\theta$, in which the secondary flow is zero. This flow has been investigated experimentally by Robinson (1973), theoretically by Moffatt (1978) and Davidson (1985), and numerically by Tacke & Schwerdtfeger (1979). We shall review some of its salient features in §3. It is shown that this type of flow is characterized by the fact that F_θ is balanced by shear, rather than inertia.

In the rest of the paper we consider a two-dimensional axisymmetric model of stirring in which F_θ is allowed to vary with z and significant secondary flows develop ($L_f \sim R$). This is a more realistic model of stirring during continuous casting. Some qualitative features of this flow have been discussed previously by Davidson & Boyson (1987).

The complex nonlinear form of the equations of motion precludes the development of an exact analytical solution in this case. However it is possible to develop an approximate 'integral-type' solution. This is discussed in §7. In §8 we shall show that this approximate solution is consistent with the results of some numerical experiments, and in §12 we compare the solution with laboratory experiments.

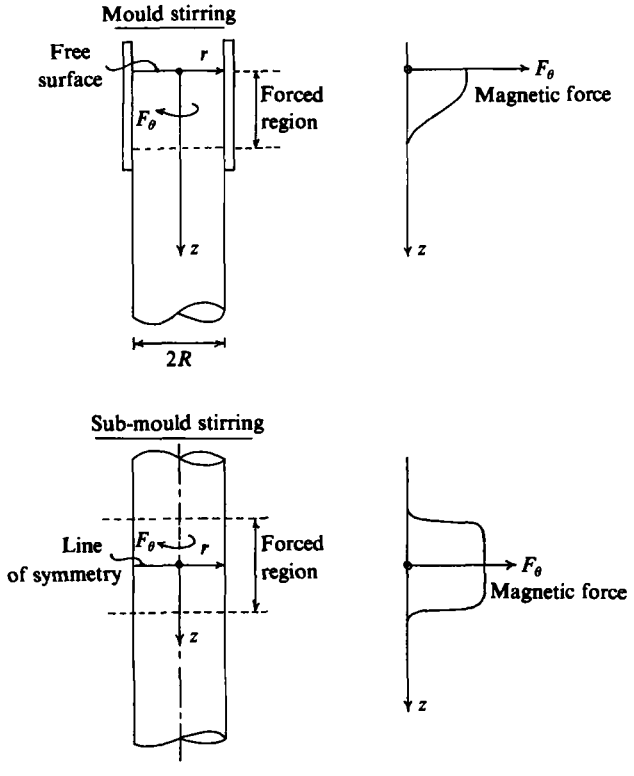

FIGURE 2. Typical magnetic body force distributions.

2. The body force induced by a rotating magnetic field

The magnetic field distribution in a liquid metal is governed by the advection–diffusion equation for $\boldsymbol{B}$

$$\frac{\partial \boldsymbol{B}}{\partial t} = \nabla \times (\boldsymbol{u} \times \boldsymbol{B}) + \frac{1}{\mu\sigma}\nabla^2 \boldsymbol{B}.$$

The relative size of the advection to diffusion terms is given by the magnetic Reynolds number

$$\mathbb{R}_m = \mu\sigma u R.$$

$\mathbb{R}_m$ is almost invariably small in industrial and laboratory electromagnetic stirring, allowing us to ignore advection of $\boldsymbol{B}$. In this approximation the fluid is treated as a stationary solid conductor.

The ratio of the time-derivative term to the diffusion term is given by the skin-depth parameter

$$\Delta = R^2\omega\sigma\mu = 2(R/\delta)^2,$$

where ω is the frequency of rotation or oscillation of $\boldsymbol{B}$, and $\delta = (2/\mu\sigma\omega)^{\frac{1}{2}}$ is the skin-depth. (Δ is sometimes given the alternative symbol $\mathbb{R}_\omega$.)

We shall look at the limiting condition where Δ is assumed to be small, although larger than $\mathbb{R}_m$

$$\mathbb{R}_m \ll \Delta \ll 1.$$

This requires the skin depth to be large relative to R, and is referred to as a low-

frequency approximation. It is shown by Tacke & Schwerdtfeger (1979) that, in the context of magnetic stirring, a low-frequency analysis can be a good approximation (to within 4%) for values of Δ as high as 2.8. Table 2 shows that, in the experiments discussed in §9 through §12, $\Delta = 2.2$. That a low-frequency analysis ($\Delta \to 0$) is a good approximation, is confirmed in §12 by comparing measurements of $\boldsymbol{B}$, with and without the liquid metal present. It is shown that $\boldsymbol{B}$ is unperturbed by the presence of the fluid.

Since we have assumed $\mathbb{R}_m \ll \Delta$, a condition almost always met in practice, we may deduce

$$u \ll \omega R.$$

This implies that the field advection term in the advection–diffusion equation for $\boldsymbol{B}$ is much smaller than the time derivative of $\boldsymbol{B}$. This is often taken as an alternative condition for the field advection term to be negligible.

The magnetic body force induced in an infinitely long metal column, of a circular cross-section, by a uniform, transverse, rotating magnetic field is well known (see, for example, Dahlberg 1972). The body force in the metal, in the low-frequency limit, is

$$F_\theta = \tfrac{1}{2}B^2\sigma\omega r.$$

There is also an oscillatory component of force, of frequency 2ω. However, this is irrotational and consequently drives no fluid motion. In §11, we shall show that, although the geometry of the magnetic field in our experiments is very different to that considered by Dahlberg (1972), the body force generated in the liquid metal is similar to the equation above, to first order in r. We shall now consider the nature of the induced body force for an arbitrary, low-frequency, rotating magnetic field.

The combined conditions of low magnetic Reynolds number and large skin depth make the expressions for the electromagnetic body force particularly simple since $\boldsymbol{B}$ remains unperturbed by either advection or time variation. The essence of the low-frequency ($\Delta \to 0$) approximation is to ignore the magnetic field generated by eddy currents and consider only an imposed irrotational field. The current density is then determined by substituting this $\boldsymbol{B}$ field into Faraday's equation and the force distribution follows. This may be shown formally by performing a perturbation analysis on the advection–diffusion equation for $\boldsymbol{B}$, in the limit of $\Delta \to 0$.

Let $\boldsymbol{B}_0$ be the imposed irrotational field, with vector potential $\boldsymbol{A}_0$. (We choose the gauge of $\boldsymbol{A}_0$ such that $\nabla \cdot \boldsymbol{A}_0 = 0$.) Faraday's equation gives the induced electric field as

$$\boldsymbol{E} = -\frac{\partial \boldsymbol{A}_0}{\partial t} - \nabla \Phi.$$

Φ is the instantaneous electrostatic potential which we may take to be zero (see Davidson 1986). The current density and body-force distribution follow from the above equation. Thus the body force may be calculated directly from $\boldsymbol{A}_0$, the imposed, free-space field. (Note that $\nabla^2 \boldsymbol{A}_0 = 0$.)

The body force $\boldsymbol{F}$ will, in general, contain both a static and an oscillatory component, at frequency 2ω. It was noted, that, for a uniform transverse field rotating about a long cylinder, the oscillatory component is irrotational and consequently drives no fluid motion. For other field geometries, however, the oscillatory component need not be irrotational. None the less, it may still be neglected, since the induced oscillatory component of velocity, u', will be significantly

smaller than the mean component, u. This may be seen by comparing inertial and electromagnetic terms in the Navier–Stokes equations

$$\rho \frac{\partial \boldsymbol{u}}{\partial t} \sim \rho \omega u' \sim \boldsymbol{F},$$

$$\rho \boldsymbol{u} \cdot \nabla \boldsymbol{u} \sim \frac{\rho u^2}{R} \sim \boldsymbol{F},$$

from which

$$\frac{u'}{u} \sim \frac{u}{\omega R}.$$

It is clear that ignoring the oscillatory components of force and velocity is consistent with our initial assumptions.

To develop an understanding of rotary electromagnetic stirring, a compromise must be sought in terms of the relative complexity of modelling. A model which is too simple may not incorporate the necessary physical processes to explain observed behaviour adequately. On the other hand, an analysis which incorporates too much detail, in terms of the magnetic field distribution or turbulent fluid motion, will lack generality in that a particular solution may only be obtained by numerical analysis.

It is apparent from a survey of the technical literature that there is a large variety of magnetic field geometries used for rotary magnetic stirring. Yet there is a requirement for a hydrodynamic analysis which has some generality, and is not restricted to a particular arrangement of inductors. Consequently, we shall look for a 'model' body-force equation which will hold true, at least approximately, in a range of magnetic field geometries.

For a low-frequency rotating field, dimensional analysis shows that the axisymmetric, steady, azimuthal component of the body force must have the general form

$$F_\theta = B^2 \sigma \omega R F\left(\frac{r}{R}, \frac{z}{R}\right).$$

Here B is a characteristic field strength, and the geometric lengthscale is taken as R. The function F is dimensionless and is of the order of unity.

We may expand $F(r/R, z/R)$ as a Taylor series about the axis $r = 0$

$$F_\theta = B^2 \sigma \omega R \left\{F_0\left(\frac{z}{R}\right) + F_1\left(\frac{z}{R}\right)\left[\frac{r}{R}\right] + F_2\left(\frac{z}{R}\right)\left[\frac{r}{R}\right]^2 + \ldots\right\}.$$

For symmetric field geometries, the even terms in this series must be zero

$$F_\theta = B^2 \sigma \omega r \left\{F_1\left(\frac{z}{R}\right) + F_3\left(\frac{z}{R}\right)\left[\frac{r}{R}\right]^2 + \ldots\right\}.$$

To first order in r/R, the body force is then

$$F_\theta = \{\tfrac{1}{2} B^2 \sigma \omega r\} f\left(\frac{z}{R}\right),$$

where

$$f\left(\frac{z}{R}\right) = 2F_1\left(\frac{z}{R}\right).$$

If $f(z/R)$ is taken as unity, then we obtain the expression given earlier for the force generated by a uniform field rotating around an infinitely long conducting cylinder.

We shall adopt the equation above as our model force and use it for the body-force term in the Navier–Stokes equation. This has the advantage that it covers the uniform field case ($f(z/R) = 1$), which is the basis of many previous studies. The disadvantage of using this equation is that, in general, it gives a poor estimate of F_θ for large r. In §11 we shall show that, for the field geometry used in the experiments, the linearization of F_θ in r leads to an overestimate of the net applied magnetic torque of about 60%.

In addition to the azimuthal force, there will, in general, be radial and axial components of force. However, these are often negligible. For example, in the case of a uniform field rotating about a long circular cylinder, F_r and F_z are zero. In the magnetic field geometry used in the experiments, F_z is shown to be zero, F_r, on the other hand, is non-zero, but only at third order in r/R (see §11).

It is convenient to introduce a characteristic velocity, $\bar{V}$, defined as

$$\bar{V} = \{B(\sigma/\rho\omega)^{\frac{1}{2}}\}\,\omega R.$$

The body-force equation then becomes

$$F_\theta = \left\{\tfrac{1}{2}\rho\left[\frac{\bar{V}}{R}\right]^2 r\right\} f\left(\frac{z}{R}\right). \tag{1}$$

It is apparent that the induced velocity scales on $\bar{V}$ when F_θ is balanced by the inertial term, $\rho\boldsymbol{u}\cdot\nabla\boldsymbol{u}$, in the Navier–Stokes equations. We shall now consider the hydrodynamic consequences of this body force.

3. One-dimensional models of stirring

We shall review briefly the nature of the flow field which results when there is no axial variation in the body force. If we take $f(z/R) = 1$ in equation (1), then

$$F_\theta = \tfrac{1}{2}\rho\left[\frac{\bar{V}}{R}\right]^2 r.$$

This force drives a one-dimensional swirl flow $u_\theta(r)$, continuity requiring the radial component of velocity to be zero. The radial component of the time-averaged Navier–Stokes equations show that the centripetal acceleration is balanced by a radial pressure gradient. The azimuthal component may be integrated to give the shear-stress distribution. Let v be the fluctuating component of velocity; then

$$\tau_{r\theta} = \rho\nu r\frac{\mathrm{d}}{\mathrm{d}r}\left[\frac{u_\theta}{r}\right] - \rho\overline{v_r v_\theta} = -\frac{1}{r^2}\int_0^r r^2 F_\theta\,\mathrm{d}r.$$

Substituting for F_θ we deduce

$$\nu r\frac{\mathrm{d}}{\mathrm{d}r}\left[\frac{u_\theta}{r}\right] - \overline{v_r v_\theta} = -\tfrac{1}{8}\bar{V}^2\left[\frac{r}{R}\right]^2. \tag{2}$$

This swirl flow is analogous to rectilinear flow in a pipe. In both situations we have an imposed shear-stress gradient. In this case the shear stress is determined by F_θ, while in pipe flow it is determined by the axial pressure gradient. The shear stress may be determined at the outset because there are no inertial effects (except for the centripetal acceleration).

For laminar flow, (2) may be integrated to give

$$u_\theta = \frac{\bar{V}^2 r}{16\nu R^2}[R^2 - r^2].$$

This well-known result shows that, in laminar flow, the velocity scales on the square of the magnetic field strength. By Rayleigh's criterion, this profile is prone to instabilities near the wall where the angular momentum is a decreasing function of radius.

Most swirling flows which occur in practice are turbulent. In a turbulent shear flow we expect u_θ to scale on the shear velocity V_*, and hence $\bar{V}$.

$$V_*^2 = \frac{|\tau_{r\theta}|_R}{\rho} = \tfrac{1}{8}\bar{V}^2.$$

Thus, in contrast to the laminar flow, the turbulent mean velocity scales linearly on field strength B.

The solution of (2) for turbulent flow requires an estimate of the Reynolds stress. A two-parameter (k, ω)-turbulence model has been used by Tacke & Schwerdtfeger (1979) to compute the flow. This assumes that the turbulent shear stress is proportional to the local mean velocity gradient and a local diffusivity. The diffusivity is calculated from the turbulence kinetic energy k and mean frequency ω. The parameters k and ω are, in turn, determined by empirical transport equations. This turbulence model is similar to the more commonly used (k, ϵ)-model (see Rodi 1984). Such an approach has the disadvantage of requiring the simultaneous solution of the Navier–Stokes equations and two subsidiary transport equations. It is therefore complex, and tends to obscure the underlying trends. An alternative approach is given by Davidson (1985) and is summarized below.

At high Reynolds numbers, gradients near the wall become sufficiently large that the fluid adjacent to the wall is approximately in a state of rectilinear motion. Since curvature effects are locally unimportant, the velocity in the inertial sublayer must have the standard logarithmic form.

$$u_\theta = V_* \left\{ 2.5 \ln\left[\frac{V_* y}{\nu}\right] + 5.5 \right\},$$

where

$$V_* = \bar{V}/2\sqrt{2}.$$

The problem is now one of extending this velocity profile into the core of the flow. We may speculate, however, that this shear flow is largely controlled by events near the wall, as in axial pipe flow. In such a situation we would expect the computed core velocity profile to be insensitive to the turbulence model used, provided that the model gives the correct velocity near the wall. The simplest turbulence model which satisfies this requirement is 'mixing length'. Application of this results in an explicit equation for the angular velocity on the axis

$$\Omega_0 = \frac{\bar{V}}{R}\left\{ 0.88 \ln \frac{\bar{V}R}{\nu} + 1.0 \right\}. \tag{3}$$

This equation is consistent with numerical experiments performed by Tacke & Schwerdtfeger (1979) using the (k, ω)-turbulence model, and compares favourably with the experimental data of Robinson (1973).

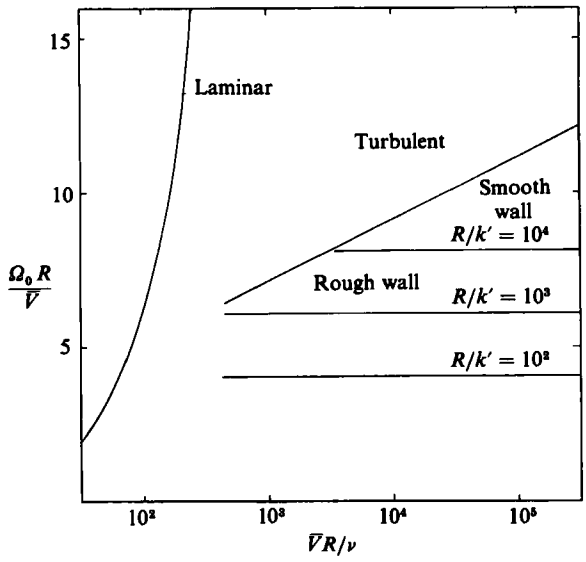

FIGURE 3. Core angular velocity for one-dimensional flow.

If the wall is rough, then the lengthscale near the wall changes from ν/V_* to k', the roughness height, and equation (3) must be replaced by

$$\Omega_0 = \frac{\bar{V}}{R}\left\{0.88 \ln \frac{R}{k'}\right\}. \tag{4}$$

It is important to distinguish between smooth- and rough-wall flow. For parameter values typical of a continuous casting plant, (4) predicts a velocity only half that predicted by (3). The difference between (3) and (4) is illustrated in figure 3.

4. Two-dimensional axisymmetric stirring – a statement of the problem

In one-dimensional flow a fluid particle experiences no azimuthal acceleration and consequently the magnetic torque must be locally balanced by shear. Unfortunately, the one-dimensional analysis is quite misleading in cases where F_θ varies with z. Consider the force distribution shown in figure 2 where the magnetic torque is applied only over a relatively short length of the column. The result of this localized forcing is differential rotation between forced and unforced regions. We shall show that, provided $\partial F_\theta/\partial z \ll F_\theta/R$, the centripetal acceleration is balanced by a radial pressure gradient. This implies the existence of an axial variation in pressure, which, in turn, drives a secondary poloidal flow. (Poloidal motion is that in the (r, z)-plane.)

We shall show that the secondary flow is as large as the primary swirl flow. Since the inertial forces are now non-zero, and the Reynolds number assumed to be large, the magnetic body force is locally balanced by inertia rather than shear. This results in a scaling law for the swirl velocity which is entirely different to that deduced from a one-dimensional model.

The analysis presented here is for laminar flow. In practice, however, most swirl flows of interest are turbulent. In order to interpret the analysis in terms of a turbulent flow, the Reynolds number should be regarded as an effective Reynolds number $\mathbb{R}_t = \bar{V}R/\nu_t$. ($\nu_t$ is an eddy viscosity.) We shall see in §8 that typical effective

Reynolds numbers $\mathbb{R}_t$ are of the order of 30. This somewhat simplistic approach may be reasonable for this flow since, as we shall show, the broad features of the flow are determined by the inertia and are insensitive to the details of the shear.

It is convenient to split the velocity field $\boldsymbol{u}$ into azimuthal $\boldsymbol{u}_\theta = (0, u_\theta, 0)$ and poloidal $\boldsymbol{u}_\mathrm{p} = (u_r, 0, u_z)$ components and examine the interaction between them

$$\boldsymbol{u} = \boldsymbol{u}_\mathrm{p} + \boldsymbol{u}_\theta.$$

Since we are considering axisymmetric flow, $\boldsymbol{\nabla}\cdot\boldsymbol{u}_\mathrm{p} = 0$.

The vorticity may be similarly divided where $\boldsymbol{\omega}_\mathrm{p} = \boldsymbol{\nabla}\times\boldsymbol{u}_\theta$ and $\boldsymbol{\omega}_\theta = \boldsymbol{\nabla}\times\boldsymbol{u}_\mathrm{p}$. Thus $\boldsymbol{u}_\theta$, or $\boldsymbol{\omega}_\mathrm{p}$, represent the primary flow, while $\boldsymbol{u}_\mathrm{p}$, or $\boldsymbol{\omega}_\theta$, represent the secondary flow.

The Navier–Stokes equation may also be split into azimuthal and poloidal components. Taking the curl of the poloidal component to eliminate pressure, we obtain

$$\boldsymbol{u}_\mathrm{p}\times\boldsymbol{\omega}_\mathrm{p} + \nu\nabla^2\boldsymbol{u}_\theta = -\frac{1}{\rho}F_\theta\hat{\boldsymbol{e}}_\theta, \tag{5}$$

$$\boldsymbol{\nabla}\times(\boldsymbol{u}_\mathrm{p}\times\boldsymbol{\omega}_\theta) + \nu\nabla^2\boldsymbol{\omega}_\theta = -\boldsymbol{\nabla}\times(\boldsymbol{u}_\theta\times\boldsymbol{\omega}_\mathrm{p}), \tag{6}$$

where

$$\boldsymbol{\nabla}\times(\boldsymbol{u}_\theta\times\boldsymbol{\omega}_\mathrm{p}) = \frac{\partial}{\partial z}\left[\frac{u_\theta^2}{r}\right]\hat{\boldsymbol{e}}_\theta. \tag{7}$$

Our formal problem is to solve these equations in a cylinder $r = R$, $z > 0$, subject to $\boldsymbol{u} = \boldsymbol{0}$ on the boundary. Equation (5) gives the azimuthal force balance. For a high Reynolds number we expect the body force to be locally balanced by the inertial term $\boldsymbol{u}_\mathrm{p}\times\boldsymbol{\omega}_\mathrm{p}$. Thus the magnetic torque is balanced by the product of the primary and secondary flows. We shall see that $\boldsymbol{u}_\mathrm{p}\times\boldsymbol{\omega}_\mathrm{p}$ represents an angular momentum flux. This is in contrast to the one-dimensional flow where the body force is balanced by the shear term $\nu\nabla^2\boldsymbol{u}_\theta$.

For a given primary flow, the secondary flow is determined by (6). This is an advection–diffusion equation for the azimuthal vorticity and corresponding poloidal velocity. It is coupled to the azimuthal velocity through the source term $\boldsymbol{\nabla}\times(\boldsymbol{u}_\theta\times\boldsymbol{\omega}_\mathrm{p})$. This represents a spiralling of the poloidal vortex lines by the azimuthal velocity, generating azimuthal vorticity. This process is illustrated in figure 4 and is the source of the secondary flow. This field-sweeping effect does not occur if u_θ is independent of z, since in such a situation the poloidal vortex lines lie parallel to the axis and u_θ is constant along a vortex line.

Equation (7) shows that the source term may be written in terms of the axial gradient of the centripetal acceleration. The explicit appearance of the centripetal acceleration is consistent with the explanation for the generation of a secondary flow given at the beginning of this section. However, since the pressure force is conservative, it is more useful to interpret the generation of secondary flow in terms of vortex sweeping.

It is useful to rewrite (5) and (6) in the following form:

$$\boldsymbol{u}\cdot\boldsymbol{\nabla}\Gamma = \nu\left\{\nabla^2\Gamma - \frac{2}{r}\frac{\partial\Gamma}{\partial r}\right\} + \frac{r}{\rho}F_\theta, \tag{8}$$

$$\boldsymbol{u}\cdot\boldsymbol{\nabla}\left(\frac{\omega_\theta}{r}\right) = \nu\left\{\nabla^2\left(\frac{\omega_\theta}{r}\right) + \frac{2}{r}\frac{\partial}{\partial r}\left(\frac{\omega_\theta}{r}\right)\right\} + \frac{\partial}{\partial z}\left(\frac{\Gamma^2}{r^4}\right). \tag{9}$$

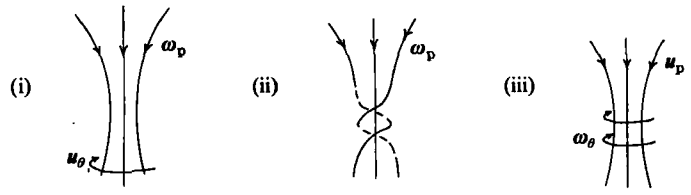

FIGURE 4. Generation of secondary flow by sweeping of poloidal vorticity.

These are scalar transport equations for ω_θ/r and $\Gamma = u_\theta r$, the angular momentum. It may be shown, by writing $\nabla \times \boldsymbol{u}_\theta$ in component form, that Γ is the stream function for the poloidal vorticity. In the absence of shear or body forces, (8) shows that Γ is advected unchanged along a streamline. This is consistent with Kelvin's circulation theorem applied to an axisymmetric material hoop.

The shear terms in the transport equations are not purely diffusive, although their effect is often diffusive in nature. This may be illustrated by considering closed streamline flow in which the body force is zero. It was shown by Batchelor (1956) that if closed streamlines exist in a region of small but finite viscosity, Γ and ω_θ/r are constant throughout that region. This is consistent with inspection of (8) and (9). Equation (8) suggests that Γ is a constant on each streamline, while the shear term causes slow diffusion of Γ between streamlines. This eventually leads to a region of constant Γ. The same argument applied to (9) suggests that ω_θ/r is constant throughout the region.

Returning to the problem in hand, (9) suggests that the secondary poloidal flow is of the form shown in figure 5. The attenuation of swirl with depth acts as a source of negative azimuthal vorticity. This is associated with a secondary flow as shown.

Equation (8) shows that the magnetic torque is balanced by a flux of angular momentum out of the forced region. Fluid entering the forced region is spun up by the body force, and the angular momentum generated here is swept into the unforced region by the secondary flow. The shear terms in (8) and (9) allow the vortex sheet, created at the wall by the no-slip condition, to diffuse into the flow. Since this is a slow process, the diffusion occurs primarily in the unforced region.

It is shown in Appendix B that the forced and diffusive regions are linked by an overlap region in which both the shear stress and the body force are negligible.

We have already noted that we expect F_θ to be balanced locally by inertia. However we cannot dispense with the shear term in (8) and (9) since they are essential for the dissipation of the energy created by F_θ. This may be illustrated by integrating the Navier–Stokes equation along a streamline to obtain a form of Bernoulli's equation

$$[p+\tfrac{1}{2}\rho u^2]_1^2 = \rho\nu \int_1^2 \nabla^2 \boldsymbol{u}\cdot \mathrm{d}\boldsymbol{r} + \int_1^2 \boldsymbol{F}\cdot \mathrm{d}\boldsymbol{r}.$$

If the integration along a streamline is taken around a closed path in the (r,z)-plane (this need not be a closed streamline since θ need not change by an integer multiple of 2π), then we deduce

$$\oint \boldsymbol{F}\cdot \mathrm{d}\boldsymbol{r} + \rho\nu \oint \nabla^2 \boldsymbol{u}\cdot \mathrm{d}\boldsymbol{r} = 0. \tag{10}$$

This states that the energy gained by a fluid particle, by virtue of the work done by

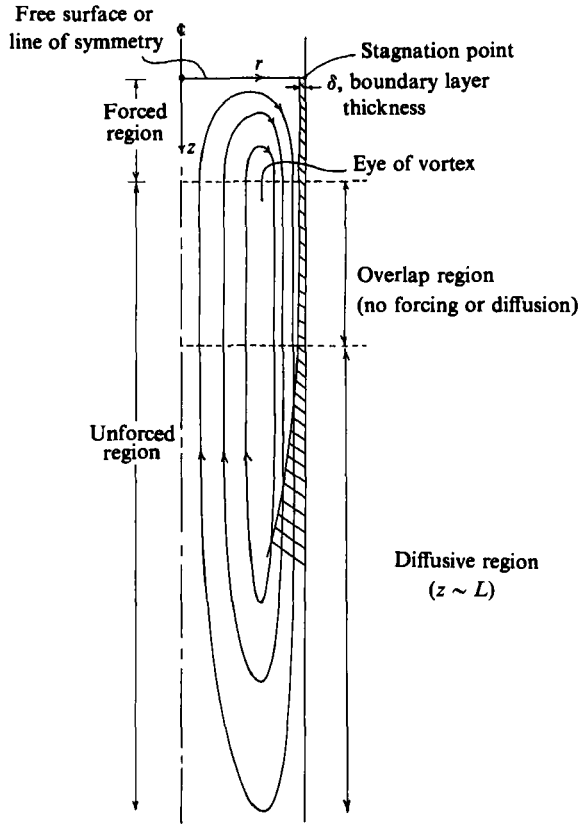

FIGURE 5. Poloidal velocity in two-dimensional stirring.

F_θ, must be diffused out of the particle by shear. Thus all streamlines must pass through a boundary layer. A similar argument may be used to show that all vortex lines must also pass through a boundary layer. Without wall shear, a forced recirculating flow cannot achieve steady state. (In the one-dimensional flow, the inertial forces are zero and the boundary-layer concept invalid; so (10) is satisfied by $u \sim 1/\nu$. For a recirculating flow, however, the requirement that $F_\theta \sim \boldsymbol{u}_p \times \boldsymbol{\omega}_p$ excludes this possibility.)

Equation (10) has implications regarding the position of the eye of the poloidal vortex and the axial lengthscale in the unforced region.

Consider first the inviscid solution of the equations of motion. The streamlines cannot be closed in the (r, z)-plane, since (10) could not then be satisfied. It follows that the only permissible inviscid solution of the equations of motion is that shown in the top half of figure 5 (marked forced region and overlap region). The streamlines are parallel to the cylinder wall at the bottom of the forced region, and remain parallel, so that the streamlines do not close. Outside the forced region the inertial forces are zero since all axial gradients are zero.

When we allow for a small but finite viscosity, we obtain the flow structure shown in figure 5. The upper half of the flow remains inviscid, to first order in $\mathbb{R}^{-1}$. However, the boundary layer, which grows from the stagnation point, will eventually turn the flow, creating a closed eddy. The lower half of the flow is diffusive in nature. It is where the energy and momentum created in the forced region is destroyed. Diffusion

becomes important in the unforced region, not because the shear terms become larger, but because the inertial terms become smaller, since, as we shall see, the axial lengthscale becomes large.

Thus we see that the eye of the poloidal vortex cannot lie in the forced region, since the flow there is essentially inviscid, but lies in the overlap region.

We may also use (10) to estimate the axial lengthscale in the unforced region. A laminar boundary layer on the wall grows at a rate

$$\delta \sim \left(\frac{\nu z}{u}\right)^{\frac{1}{2}}.$$

Since each streamline must pass through this boundary layer, this suggests that the axial lengthscale in the diffusive region, L, may be obtained by substituting $\delta \sim R$ and $z \sim \mathrm{L}$ into this equation, giving

$$L \sim \mathbb{R} \times R. \tag{11}$$

This result implies that the swirl penetrates well beyond the immediate vicinity of the forced region.

If (8) is integrated over a volume bounded by $r = 0$, $r = R$, $z = 0$ and $z = z_0$, we obtain an angular momentum integral. If T_z is the net torque applied to the control volume (magnetic plus shear), then

$$T_z = 2\pi\rho \int_0^R \Gamma r u_z \, \mathrm{d}r. \tag{12}$$

The integral on the right of this expression is the flux of angular momentum through the surface $z = z_0$. If we take $z_0 = \infty$, so that the control volume is the whole flow field, then the applied magnetic torque is balanced by shear on the walls

$$\int_0^\infty \int_0^R F_\theta r^2 \, \mathrm{d}r \, \mathrm{d}z = R^2 \int_0^\infty |\tau_{r\theta}|_R \, \mathrm{d}z.$$

We now take z_0 to coincide with the bottom of the forced region, or more precisely, to lie in the overlap region. We may neglect wall shear in the forced region in comparison with the total wall shear. If $\bar{u}_\theta$ and $\bar{u}_z$ are velocity components at the bottom of the forced region, then

$$\int_0^\infty \int_0^R F_\theta r^2 \, \mathrm{d}r \, \mathrm{d}z = \rho \int_0^R r^2 \bar{u}_\theta \bar{u}_z \, \mathrm{d}r.$$

If we now combine these two results, and substitute for F_θ using (1), we obtain

$$\tfrac{1}{8}\bar{V}^2 R^2 \int_0^\infty f\left(\frac{z}{R}\right) \mathrm{d}z = \int_0^R r^2 \bar{u}_\theta \bar{u}_z \, \mathrm{d}r = R^2 \int_0^\infty \frac{|\tau_{r\theta}|_R}{\rho} \mathrm{d}z. \tag{13}$$

This shows that the total applied magnetic torque is equal to the flux of angular momentum out of the forced region, which in turn is equal to the torque due to wall shear. Equation (13) may be used as a basis for dimensional analysis. We shall consider the forced and unforced regions separately.

Forced Region: Comparing inertial terms in (9) we deduce that, $u_z \sim u_\theta$, while comparing the first two terms in (13), we see that $u_\theta u_z \sim \bar{V}^2$. In addition, the

continuity equation gives us $u_r \sim u_z$; thus we have the following scaling law in the forced region:

$$u_r \sim u_\theta \sim u_z \sim \bar{V}.$$

Note that the secondary flow is as large as the primary flow.

Unforced Region: Compatibility of the forced and unforced regions requires $u_\theta \sim u_z \sim \bar{V}$, while comparing the first and last terms in (13) we find $\bar{V}^2 R^3 \sim R^2 \nu (u_\theta / R) L$. In addition, the continuity equation gives, $u_r/R \sim u_z/L$. Introducing a Reynolds number

$$\mathbb{R} = \frac{\bar{V} R}{\nu},$$

we deduce the following scaling laws in the unforced region,

$$u_\theta \sim u_z \sim \bar{V}, \quad u_r \sim \bar{V}/\mathbb{R}, \quad L \sim \mathbb{R} \times R.$$

Note that this estimate of the axial lengthscale L is the same as that given by (11).

These results are only valid if the fluid is allowed to develop its natural lengthscale L. If the column is truncated, so that the poloidal flow is mechanically forced to recirculate prematurely, then diffusion processes do not have time to act on the fluid in the unforced region. The nature of the flow is then completely transformed. This is considered briefly in §8, and in more detail in Davidson (1986).

5. Symmetry of the flow and the form of the inviscid solution

It has been assumed that the axial lengthscale in the forced region is R, and shown that the resulting axial lengthscale in the unforced region is $\mathbb{R} \times R$. It follows that axial derivatives in the unforced region are negligible, while those in the forced region are of the same order as the radial gradients. However, in typical magnetic stirring applications where $L_f \approx R$ we shall see that, in both numerical and laboratory experiments, axial derivatives in the forced region are significantly smaller than radial gradients. This is illustrated, for example, in figure 9 which shows the axial variation in computed angular velocity. These gradients are dictated by the spatial distribution of the body force. If the axial rate of decay of the body force is sufficiently rapid, then we would not expect the axial gradients to be small. We shall make the assumption $\partial u/\partial z \ll \partial u/\partial r$ in the analysis which follows. This allows some convenient simplifications in the equations of motion, although this does place a restriction on the axial variation of the body force, $f(z/R)$. (Note that if axial gradients are small, then continuity gives us, $u_r \ll u_z$.)

When axial derivatives are neglected, the azimuthal vorticity is given by

$$\omega_\theta = -\frac{\partial u_z}{\partial r}.$$

The equations of motion (8) and (9) become

$$\boldsymbol{u} \cdot \nabla \Gamma = \nu \left\{ r \frac{\partial}{\partial r} \left(\frac{1}{r} \frac{\partial \Gamma}{\partial r} \right) \right\} + \frac{1}{\rho} r F_\theta, \tag{14}$$

$$\boldsymbol{u} \cdot \nabla \left[\frac{\omega_\theta}{r} \right] = \nu \left\{ \frac{1}{r^3} \frac{\partial}{\partial r} \left(r^3 \frac{\partial}{\partial r} \left(\frac{\omega_\theta}{r} \right) \right) \right\} + \frac{\partial}{\partial z} \left(\frac{\Gamma^2}{r^4} \right), \tag{15}$$

$$\frac{\partial p}{\partial r} = \rho \frac{u_\theta^2}{r}.$$

The last equation is derived from the radial component of the Navier–Stokes equations and allows the pressure distribution to be calculated once the angular velocity is determined.

It is convenient to introduce the Stokes stream function ψ to satisfy continuity of the poloidal velocity

$$u_r = -\frac{1}{r}\frac{\partial \psi}{\partial z}, \quad u_z = \frac{1}{r}\frac{\partial \psi}{\partial r}.$$

We may expand ψ and Γ as power series in r about the axis

$$\psi = \sum_{n=1}^{\infty} g_n(z)\, r^n$$

$$\Gamma = \sum_{n=1}^{\infty} h_n(z)\, r^n$$

If these are substituted into the transport equations, and coefficients of r^n equated to zero, we obtain a series of recurrence equations for the coefficient functions $g_n(z)$ and $h_n(z)$. Provided the shear terms are retained in the original equations, it may be shown that ψ and Γ are both even in r. We therefore introduce a new variable s defined as

$$s = r^2.$$

When written in terms of s, the transport equations are simplified.

If we restrict attention to the forced region, then we may drop the shear terms in (14) and (15) along with the corresponding no-slip boundary conditions. In order to obtain a universal solution of the transport equations, for all forms of $f(z)$, it is convenient to introduce a 'stretch variable' p for the forced region, defined as

$$p = \frac{\int_0^z f\left(\frac{z}{R}\right) \mathrm{d}z}{\int_0^\infty f\left(\frac{z}{R}\right) \mathrm{d}z}. \tag{16}$$

The inviscid equations of motion become

$$\left\{-\frac{\partial \psi}{\partial p}\frac{\partial}{\partial s} + \frac{\partial \psi}{\partial s}\frac{\partial}{\partial p}\right\}\Gamma = \frac{\bar{V}^2}{4R^2} s \int_0^\infty f\left(\frac{z}{R}\right) \mathrm{d}z \tag{17}$$

$$\left\{-\frac{\partial \psi}{\partial p}\frac{\partial}{\partial s} + \frac{\partial \psi}{\partial s}\frac{\partial}{\partial p}\right\}\left[\frac{\partial^2 \psi}{\partial s^2}\right] = -\frac{1}{8s^2}\frac{\partial \Gamma^2}{\partial p}. \tag{18}$$

The axial coordinate z does not appear explicitly in these equations, except as a dummy variable. In addition, the depth function $f(z/R)$ does not appear, except in the integral (which we could normalize as unity). It follows that, provided F_θ is linear in r, there is a universal solution to the inviscid equations for Γ and ψ in the independent variables s and p.

One result of introducing the variable p is that the region lying between the bottom of the forced region and $z \to \infty$ is compressed onto the surface $p = 1$.

6. Some features of the flow in the overlap region

It is shown in Appendix B that, to accommodate the change in axial lengthscale, the flow in the overlap region is almost parallel, axial derivatives being zero to first order in $\mathbb{R}^{-1}$. It is also shown that this overlap region is essentially unforced and inviscid (to first order in $\mathbb{R}^{-1}$).

The numerical experiments described in §8 show that, at the bottom of the forced region, u_θ is linear in r, and u_z parabolic in r

$$u_\theta = \Omega r, \tag{19}$$

$$u_z = \tfrac{1}{4}c(R^2 - 2r^2), \quad \text{i.e. } \frac{\omega_\theta}{r} = c, \tag{20}$$

where Ω and c are constants. Note that (20) implies that the eye of the vortex lies at $r = R/\sqrt{2}$.

These velocity profiles are interesting in that they are the only kinematically allowable profiles which reduce to zero the diffusion terms in the transport equations (14) and (15). Thus the overlap region is one in which ω_θ/r and u_θ/r are constant, and the shear terms in the transport equations are zero. This is similar to the situation described by Batchelor (1956), suggesting that the explanation for the observations may lie in the radial diffusion of angular momentum and azimuthal vorticity between streamlines. However, it is essential to Batchelor's analysis that the streamlines be closed in a region of small viscous and magnetic forces. This is not the case here. In addition, Batchelor's analysis predicts a free vortex, whereas we observe a forced vortex.

An alternative explanation of (19) and (20) is that $\partial u_\theta/\partial z$ and $\partial u_z/\partial z$ may be zero to second order in $\mathbb{R}^{-1}$ in the overlap region. This would ensure that the inertial forces are zero to second order in $\mathbb{R}^{-1}$, and consequently that the shear terms are zero to first order. Equations (19) and (20) would then follow.

It is interesting to note that, in the numerical and physical experiments described in §8 and §12, u_θ and $|u_z|$ are observed to have maxima, with respect to z, in the overlap region. It is possible to explain the existence of the maxima in u_θ and $|u_z|$ by an interpretation of the flow-field geometry. That $|u_z|$ exhibits a maximum at the bottom of the forced region follows from the fact that across the eye of the eddy $u_r = 0$ (parallel flow). That u_θ should exhibit a maximum is less clear. However, it is shown in Appendix A that it is a feature of the inviscid equations of motion that u_θ increases with depth from the surface down to the bottom of the forced region. We expect, however, that in the unforced region u_θ will decay with depth. It follows that u_θ must have a maximum in the vicinity of the bottom of the forced region. (It is somewhat surprising that the swirl is largest at the very point at which the driving force drops to zero.) Note, however, that the existence of these maxima does not ensure that $\partial u_\theta/\partial z$ and $\partial u_z/\partial z$ are zero to second order (in $\mathbb{R}^{-1}$) throughout the overlap region, and therefore does not explain (19) and (20).

7. An approximate solution to the flow in the forced region

In this section we shall consider constructing an approximate solution to the transport equations. We shall incorporate into the solution the observed feature that u_z is parabolic in r, and u_θ linear in r in the overlap region.

We expect that the velocity components have a relatively simple functional dependence on r. This suggests that they could be reasonably approximated by low-

order polynomials in r. Consequently we look for an approximate solution of the form shown below. (It is convenient to use the dimensionless variables introduced in Appendix B where $\hat{\psi} = \psi/\bar{V}R^2$, $\hat{\Gamma} = \Gamma/\bar{V}R$, $\hat{s} = s/R^2$, and $X = z/R$)

$$\hat{\psi} = \tfrac{1}{2}u_0(p)\,\hat{s}(1-\hat{s}), \tag{21}$$

$$\hat{\Gamma} = \Omega_1(p)\,\hat{s} + \Omega_3(p)\,\hat{s}^2, \tag{22}$$

where $\Omega_3(1) = 0$, $u_0(0) = 0$.

These may be regarded as Maclaurin series for ψ and Γ in which terms of order r^6, and higher, are discarded. Expressions (21) and (22) satisfy the boundary conditions,

$$\psi = 0 \quad \text{on } s = 0, R^2, \quad z = 0,$$

$$\Gamma = 0 \quad \text{on } s = 0.$$

By ensuring $\Omega_3(1) = 0$ we have incorporated the empirical observation that u_θ is linear in r in the overlap region. We must choose the dimensionless functions u_0, Ω_1 and Ω_3 to satisfy some aspects of transport equations (17) and (18). Since u_0 and Ω_1 are the first terms in a power series expansion about $r = 0$, we will choose these functions to satisfy the equations of motion near the axis. Substituting (21) and (22) into the equations of motion, and letting s tend to zero, we obtain

$$u_0\Omega_1'(p) - \Omega_1 u_0'(p) = \frac{1}{2}\int_0^\infty f(X)\,\mathrm{d}X \tag{23}$$

$$2u_0\,u_0'(p) = \Omega_1\,\Omega_1'(p). \tag{24}$$

We now choose Ω_3 to satisfy the angular momentum integral (12). This ensures that, at any given depth z_0, the net magnetic torque applied to the fluid in $0 < z < z_0$ is equal to the net flux of angular momentum across the surface $z = z_0$. Substituting the expressions for ψ and Γ into (12) gives

$$u_0(\Omega_1 + \Omega_3) = -\frac{3}{2}\int_0^\infty f(X)\,\mathrm{d}X\,p. \tag{25}$$

Solving (23), (24) and (25) subject to the boundary conditions $u_0(0) = 0$, $\Omega_3(1) = 0$, we obtain

$$u_0(p) = -\frac{1}{\sqrt{2}}\Omega_s \sinh(\sqrt{2}p), \tag{26}$$

$$\Omega_1(p) = \Omega_s \cosh(\sqrt{2}p), \tag{27}$$

$$\Omega_3(p) = \Omega_s\left\{3\frac{\sqrt{2}p}{\sinh(\sqrt{2}p)} - \cosh(\sqrt{2}p)\right\}, \tag{28}$$

where

$$\Omega_s^2 = \frac{1}{2}\int_0^\infty f(X)\,\mathrm{d}X. \tag{29}$$

Note that Ω_1 is an increasing function of z which is consistent with the analysis given in Appendix A.

The velocity components u_θ and u_z are given by

$$u_z = \bar{V}u_0(p)[1-2\eta^2], \tag{30}$$

$$u_\theta = \bar{V}[\Omega_1(p)\,\eta + \Omega_3(p)\,\eta^3], \tag{31}$$

where $\eta = r/R$.

Note that (30) implies that the eye of the poloidal vortex lies at $\eta = 1/\sqrt{2}$.

We now compare this solution with numerical experiments performed on the Reynolds-averaged Navier–Stokes equations, with approximations for the Reynolds stresses.

8. A comparison of the approximate solution for two-dimensional stirring with numerical experiments

We shall compare the results of §7 with some computations of turbulent flow. There are two reasons for wishing to compute turbulent, rather than laminar, flow. Firstly, nearly all swirling flows of interest in practice are turbulent. The second reason is that the laminar solution is probably unstable by Rayleigh's criterion ($\partial\Gamma/\partial r < 0$) for high Reynolds numbers. (There is a disadvantage, however, in computing turbulent flow, in that, since $\mathbb{R}_t \sim 30$, the asymptotic boundary-layer theory is not strictly valid.)

The Reynolds stresses are estimated using the standard (k, ϵ)-model described by Rodi (1984). This is an eddy viscosity model of turbulence in which the Reynolds stresses are proportional to the rate of strain. The eddy viscosity ν_t is related to the turbulence kinetic energy k and viscous dissipation, ϵ. The (k, ϵ)-model proposes transport equations for both k and ϵ. The transport equation for k is based on the turbulence kinetic energy equation, while the transport equation for ϵ is empirical. There is some debate regarding the generality and validity of the ϵ equation, and consequently the (k, ϵ)-model must be used with caution. We expect, however, that the flow in the forced region is largely controlled by the inertia of the mean flow, and therefore is insensitive to the details of the shear.

The computations were performed using a finite-difference code employing a power-law differencing scheme, described by Patankar (1980). The body force is that given by equation (1), with a fourth power-law decay for $f(X)$

$$f(X) = 2[1 + X^4]^{-1}.$$

The effective depth of stirring is $X \approx 2.3$, corresponding to the force having dropped to 3% of its original value. This figure of 3% is chosen to define the edge of the forced region since an appropriate cutoff criterion is $\mathbb{R}_t^{-1}$ (see Appendix B), and we shall see that $\mathbb{R}_t \sim 30$. However, since the drop-off rate for F_θ is rapid ($F_\theta \sim X^{-4}$), the effective depth of stirring is insensitive to the exact interpretation of what constitutes an insignificant level of force.

It is predicted in the analysis of §4 that the velocity in the forced region should scale linearly on $\bar{V}$, and be independent of wall shear. In order to test this hypothesis, two different cases were computed, corresponding to different magnitudes of body force

$$F_\theta = \tfrac{1}{2}\rho \left[\frac{\bar{V}}{R}\right]^2 r f\left(\frac{z}{R}\right).$$

In the first case F_θ was chosen such that $\bar{V} = 1$ cm/s, while in the second case F_θ was calculated using $\bar{V} = 10$ cm/s. We shall see that the computed velocities in the two cases are almost identical in distribution and a factor of 10 different in magnitude. In order to confirm that this scaling is independent of wall shear, significant wall roughness was introduced in the second case. The wall roughness is specified in terms of a roughness parameter $E = \nu/V_* k'$, where k' is the roughness height (see Rodi 1984). A value of $E = 0.1$ was chosen which corresponds, approximately, to $k' = 0.5$ mm for the Reynolds number used.

Case	ρ (kg/m^3)	ν (m^2/s)	R (m)	$\bar{V}$ (m/s)	$\mathbb{R} = \bar{V}R/\nu$	Wall roughness k' (m)
1	7×10^3	10^{-6}	0.1	0.01	10^3	0
2	7×10^3	10^{-6}	0.1	0.1	10^4	0.5×10^{-3}

TABLE 1. Physical properties used in the computations

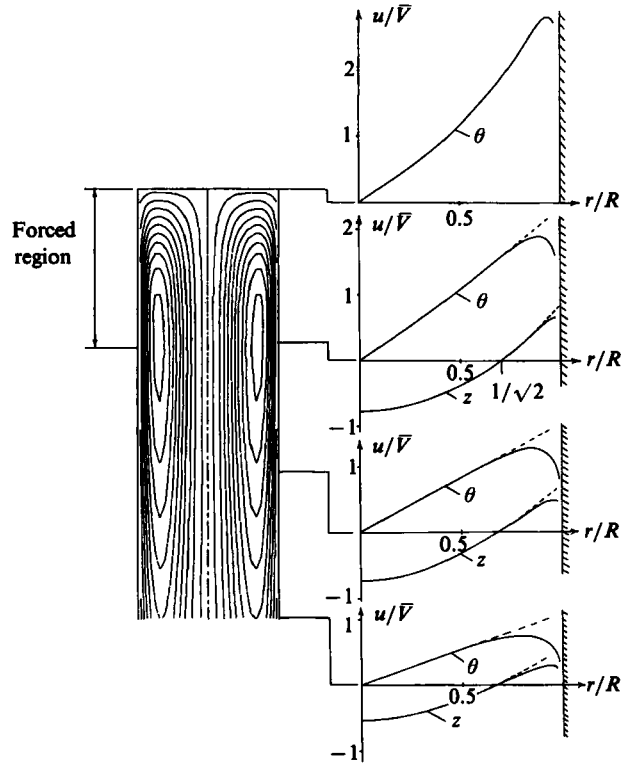

FIGURE 6. Computed poloidal flow pattern and velocity profiles for case 1.

The radius of the column was chosen to be 10 cm. Details of the relevant physical properties used in the computations are given in table 1.

In both the cases analysed the radial velocity was found to be of the order of $\frac{1}{10}\, u_z$, even in the forced region. Since $\nabla \cdot \boldsymbol{u}_p = 0$, this confirms that axial derivatives are significantly smaller than radial derivatives, an assumption made in the previous section.

Figure 6 shows part of the computed poloidal flow pattern and some representative velocity profiles for the smooth-wall case. The difference between the axial and radial lengthscales, particularly in the unforced region, is clear. The eye of the poloidal vortex lies at,

$$z_0 = 2.5R, \quad r_0 = 0.71R.$$

In the case of the rough-wall flow, the eye of the vortex lies at

$$z_0 = 2.2R, \quad r_0 = 0.70R.$$

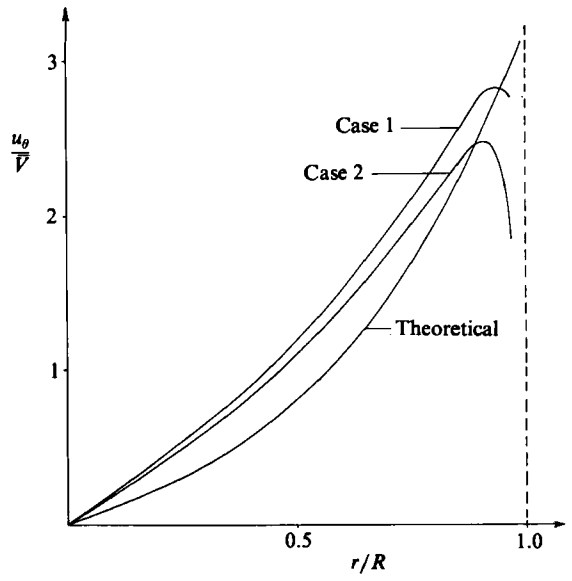

FIGURE 7. Comparison of computed and theoretical swirl velocities, ($z = 0$). Case 1, smooth wall $\mathbb{R} = 10^3$; case 2, rough wall $\mathbb{R} = 10^4$.

In both flows $\partial u_z/\partial z$ was found to be zero at $z = z_0$, corresponding to $u_r(r, z_0) = 0$ (parallel flow).

These computed results should be compared with the theoretical predictions of §4 and equation (20) for the position of the vortex eye

$$z_0 \approx 2.3R \quad \text{(bottom of the forced region)},$$

$$r_0 = \frac{1}{\sqrt{2}} R \quad \text{(parabolic profile for } u_z\text{)}.$$

For both cases analysed, the computed axial velocity profile at the bottom of the forced region $u_z(r, z_0)$ deviated from the parabola given by (20) by no more than 4% (excluding the boundary layer).

Figures 7 and 8 compare theoretical and computed velocity profiles for u_θ at the plane of symmetry ($z = 0$) and approximately at the bottom of the forced region ($z = 2.2R$). Note the u_θ is approximately linear in figure 8. There is a reasonable correspondence between the computed profiles and the approximate solution given by (26) to (31). Clearly u_θ scales on $\bar{V}$.

The computed eddy viscosity varies throughout the flow field. Near the wall, it increases linearly with distance from the wall. In the core, ν_t is approximately constant, decaying slowly with depth. Based on a core eddy viscosity, $\mathbb{R}_t = \bar{V}R/\nu_t \sim 30 \rightarrow 40$ for both the smooth- and rough-wall flows.

One feature of the flow which is given by the computations, but not the analysis in §7, is the penetration of the swirl beyond the forced region. Figure 9 shows the variation of core angular velocity with depth for both cases. The swirl extends well out of the stirred region. It is clear from a comparison of this figure with figures 7 and 8 that axial gradients in u_θ are very much smaller than radial gradients, even in the forced region. This is also observed in the laboratory experiments.

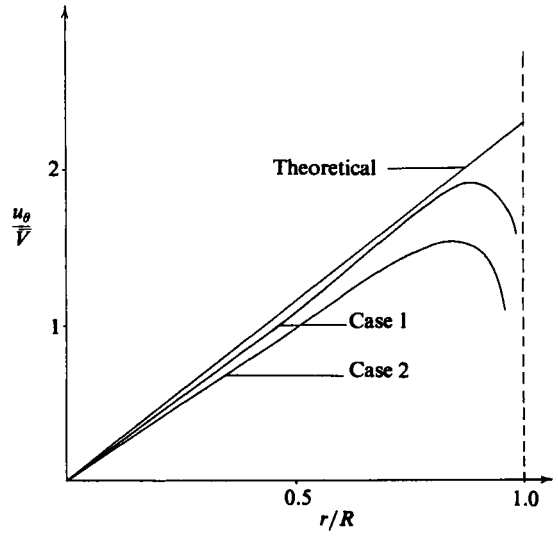

FIGURE 8. Comparison of computed and theoretical swirl velocities, ($z = 2.2R$). Case 1, smooth wall $\mathbb{R} = 10^3$; case 2, rough wall $\mathbb{R} = 10^4$.

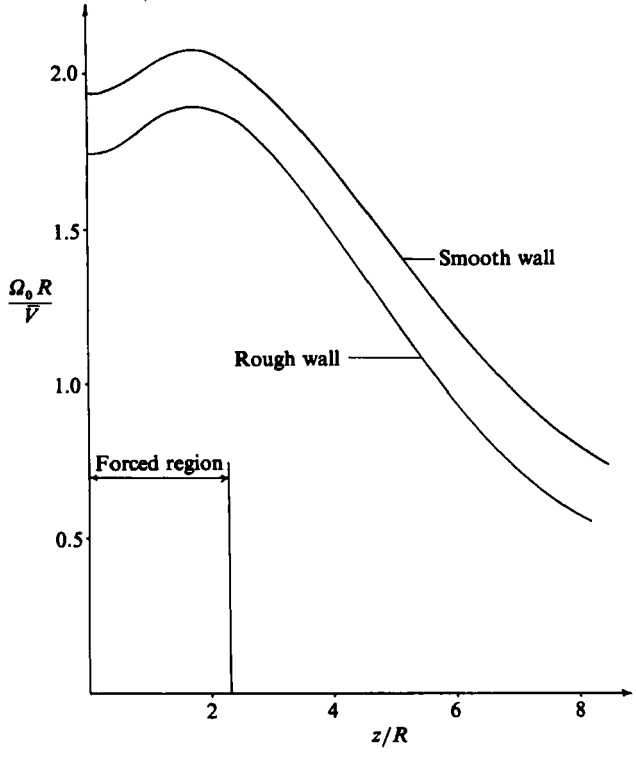

FIGURE 9. Axial variation of computed core angular velocity.

Another interesting feature of this figure is that the core angular velocity increases with depth from the surface to the bottom of the forced region. This is consistent with the analysis of Appendix A and indicates that inertia is indeed dominant in the forced region. This behaviour is also seen in the physical experiments. Appendix A also shows that, based on an inviscid analysis, u_θ should be an increasing function of depth near the wall. Unfortunately, this cannot be confirmed by the computations because of the intrusion of the boundary layer on the inviscid velocity profile.

It is of some interest to investigate what occurs if the flow is prevented from adopting its natural recirculating lengthscale, $L = \mathbb{R}_t R$. This is what happens when swirl is generated in a finite-length cylinder. The endwalls mechanically force the flow to recirculate prematurely and the diffusion processes which normally occur in the unforced region do not have time to act fully on the fluid.

Some preliminary numerical experiments were performed on finite-length cylinders. These are discussed in detail in Davidson (1986). It was found that the introduction of an endwall substantially alters the structure of the flow field. The angular momentum is larger, and the secondary flow smaller, in a finite-size vessel than in the corresponding infinite vessel. That the swirl is increased seems plausible, since angular momentum does not have time to diffuse from a fluid particle to the sidewall as it recirculates through the unforced region. The fluid particle thus has a higher swirl velocity on its arrival back at the forced region. An alternative way of explaining why u_θ must be higher in a truncated cylinder is to consider the overall torque balance. Since the swirl does not extend over its natural length, $L = \mathbb{R}_t R$, the fluid must spin faster to produce the same net wall shear required to balance the applied magnetic torque.

Having established that the swirl is larger in a truncated cylinder, it is possible to explain, at least qualitatively, why the secondary flow is smaller. We have seen that the applied magnetic torque is locally balanced by a flux of angular momentum out of the forced region. This angular momentum flux, $\boldsymbol{u}\cdot\nabla\Gamma$, is the product of the swirl and the secondary flow. It follows, therefore, that if the swirl is increased, then the secondary flow must decrease.

It is not only the magnitude of the velocity components which are altered, but also the distribution of velocity. In the infinite cylinder case, the axial velocity is parabolic in r throughout most of the forced region. When the cylinder is truncated, however, we get a different profile. The core axial velocity becomes more uniform, decreasing in magnitude, and the eye of the vortex moves closer to the wall. The axial flow near the wall begins to resemble that of a wall jet.

It is obviously important to distinguish clearly between infinite and finite cylinder flows. We shall now consider some laboratory experiments of magnetically-driven swirl.

9. Nature of the laboratory experiments

The one-dimensional swirl flow of liquid metal, driven by magnetic forces, has been studied experimentally by Robinson (1973) and Tacke & Schwerdtfeger (1979). Both compared their experimental results with computations performed using eddy-viscosity models of turbulence. They found a reasonable correspondence between experiment and computation, (to within 30% in the latter case). In our experiment, we extend this work to include secondary flow, by introducing an axial variation in the magnitude of the body force. This flow is precisely that encountered in the electromagnetic stirring of continuously cast steel.

The main points which are looked at in the experiments are:

(i) the scaling law for the swirl. In particular, does u_θ scale on $\bar{V}$, as predicted in §4?

(ii) the position of maximum swirl. This is predicted in Appendix A to occur at the bottom of the forced region;

(iii) the penetration of swirl outside the forced region, and its rate of decay with depth. (The axial lengthscale in the unforced region is predicted in §4 to be of the order of $\mathbb{R}_t R$, where $\mathbb{R}_t = \bar{V}R/\nu_t \approx 30$ for typical geometries.)

The local azimuthal velocity is measured using a drag probe, and the mean core rotation rate (averaged over a 46 mm radius) is measured using a rotating vane. The drag probe is similar to that used by Moore (1982) to study induction-furnace flows. The designs of the drag probe and rotating vane, and the errors involved in using these instruments, are discussed in detail in Davidson (1986).

Several problems arose in taking and analysing these measurements. Firstly, the magnetic stirrer used has been empirically developed for industrial use, and generates a complex three-dimensional magnetic field. Some modelling of the behaviour of the stirrer is required in order to calculate the applied body force. In addition, it was found that the body force $\boldsymbol{J} \times \boldsymbol{B}$ has a non-axisymmetric component, and is not linear in r throughout the range $0 < r < R$. Axial symmetry and a linear variation of $\boldsymbol{J} \times \boldsymbol{B}$ in r had both been assumed in the earlier analysis. We shall show that the latter effect is especially important, since a theoretical estimate of the total applied magnetic torque, based on an assumed linear variation of $\boldsymbol{J} \times \boldsymbol{B}$ with r, may overestimate the true torque by as much as 60% in this case.

There were also difficulties in measuring low mean velocities, (below about 0.1 m/s) so that the extent of the swirl below the forced region could not be measured accurately. This was accentuated by the tendency of the vortex core to precess in an unsteady manner, a characteristic feature of swirl flows (see Gupta, Lilley & Syred 1984).

These problems make a direct comparison between theory and experiment difficult. Consequently, in comparing the measurements with the theory, the main emphasis is on the structure of the flow and on the scaling law for the velocity.

10. Design of the experiment

A copper tube containing mercury had a magnetic stirrer mounted at its top, as shown in figure 10. The copper tube had an internal radius of 72.5 mm and a depth of 800 mm. The body force generated by the stirrer is limited to a relatively shallow surface layer of mercury. The field frequency is 50 Hz.

It was decided to simulate a rough surface on the bore of the cylinder for two reasons. First, during the stirring of cast steel, the melt sees the dendritic surface of the solidifying steel. This surface is rough, with a typical roughness depth of about 1 mm. The second reason is that swirl will penetrate a distance from the surface which is of the order of $\mathbb{R}_t \times R$. Thus, to simulate stirring of a semi-infinite column, a deep tube is required. The tube used here has a depth of $\sim 11R$, and some preliminary tests with a smooth bore showed that the swirl velocity was still significant in the vicinity of the base plate. However, introducing a rough surface has the effect of increasing the eddy viscosity and hence reducing the effective Reynolds number. The net result is a reduction in the penetration of swirl below the surface. With a rough surface, the swirl was found to decay to almost zero near the base plate, thus simulating semi-infinite stirring.

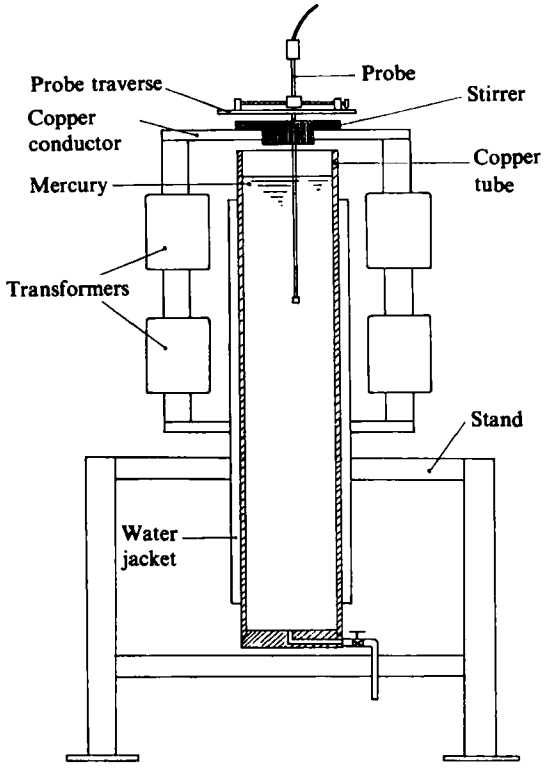

FIGURE 10. Experimental rig.

Table 2 shows characteristic values for the physical parameters of the experiment. For comparison, the equivalent values in a typical industrial steel stirrer are given.

The magnetic stirrer used here was developed for commercial use by T.I. Research Laboratories (TIRL). It generates a rotating magnetic field above the surface of the liquid metal, and relies on the fringing of this field onto the liquid surface to produce rotation.

An idealization of the stirrer is shown in figure 11. The currents in the four limbs of the copper square are separated in phase by 90°. The stirrer is designed to generate two, two-dimensional, fringing fields, oscillating 90° out of phase and mutually perpendicular. This produces a pseudo-rotating field as shown in figure 11. The magnetic field is inevitably more complex and fully three-dimensional than the biplanar distribution shown in this figure. However, measurements show that the biplanar model is a good approximation throughout most of the fluid, and we shall adopt this model here. The errors resulting from this approximation are considerably less than the error involved in linearizing F_θ in r about the axis, and therefore are acceptable.

We shall now consider the shape of the two-dimensional field generated by opposite pole pieces. For simplicity, the only sources of magnetic flux are assumed to be the pole piece faces. Adopting the low-frequency approach outlined in §2, we may ignore attenuation of the magnetic field by eddy currents in the fluid. The problem then becomes that of plotting the free-space magnetic field ($\nabla \cdot \boldsymbol{B} = 0$, $\nabla \times \boldsymbol{B} = \boldsymbol{0}$) generated by two magnetic-flux sources, A and D in figure 11, and two

Parameters	Symbol	Units/groups	Value in experiment (mercury at 20 °C)	Value in a typical stirring application (steel at 1600 °C)
Physical constants				
Radius	R	cm	7.25	10
Density	ρ	kg/m^3	13.55×10^3	7.07×10^3
Conductivity	σ	Ω^{-1} m^{-1}	1.05×10^6	0.715×10^6
Viscosity	ν	m^2/s	0.115×10^{-6}	0.886×10^{-6}
Meniscus level field strength	B	Gauss	300	300
Derived groups				
Skin depth in fluid at 50 Hz	δ	$\left(\frac{2}{\sigma\omega\mu}\right)^{\frac{1}{2}}$ (cm)	6.95	8.42
Hartmann number	Ha	$BR\left(\frac{\sigma}{\rho\nu}\right)^{\frac{1}{2}}$	56	32
Characteristic velocity	$\bar{V}$	$B\left(\frac{\sigma}{\rho\omega}\right)^{\frac{1}{2}}\omega R$ (cm/s)	34	53
Reynolds number	$\mathbb{R}$	$\bar{V}R/\nu$	0.21×10^6	0.06×10^6

TABLE 2. Characteristic parameters of the experiment

magnetic-flux sinks, B and C. The simplest boundary condition on the field is to regard the tube wall as perfectly conducting ($\boldsymbol{B}\cdot\boldsymbol{n}=0$), and take it to be in line with the pole piece faces as shown in figure 11. (Strictly, this is only valid if the tube has a square cross-section.)

There is no flux linkage between the top pole pieces, B and D, since there is a low-reluctance mild-steel path provided between them (not shown in figure 11). The flux prefers to take the low-reluctance path rather than the high-reluctance air gap across the tube.

We may introduce a vector and scalar potential for $\boldsymbol{B}$. In two dimensions, say the (x,y)-plane, this takes the form

$$\boldsymbol{B}=-\nabla\phi=\nabla\times(-\psi\boldsymbol{k}).$$

(For the present purposes, the x and y coordinates lie in the vertical plane shown in the top view of figure 11.) ψ is the streamfunction of the field. It is convenient to introduce the complex potential,

$$F(\bar{z})=\phi+\mathrm{j}\psi \quad \text{where } \bar{z}=x+\mathrm{j}y.$$

The complex potential for a source q, discharging into a channel of width a, is given by Lamb (1959),

$$F(\bar{z})=-\frac{q}{\pi}\ln\sinh\left(\frac{\pi\bar{z}}{2a}\right).$$

Using this potential, one can introduce distributed sources at A and D and distributed sinks at B and C. The potential for these distributed sources and sinks is given in Davidson (1986). By symmetry, the strengths of the source and sink at A and C are equal, as are those at D and B. However, the top pole pieces have a

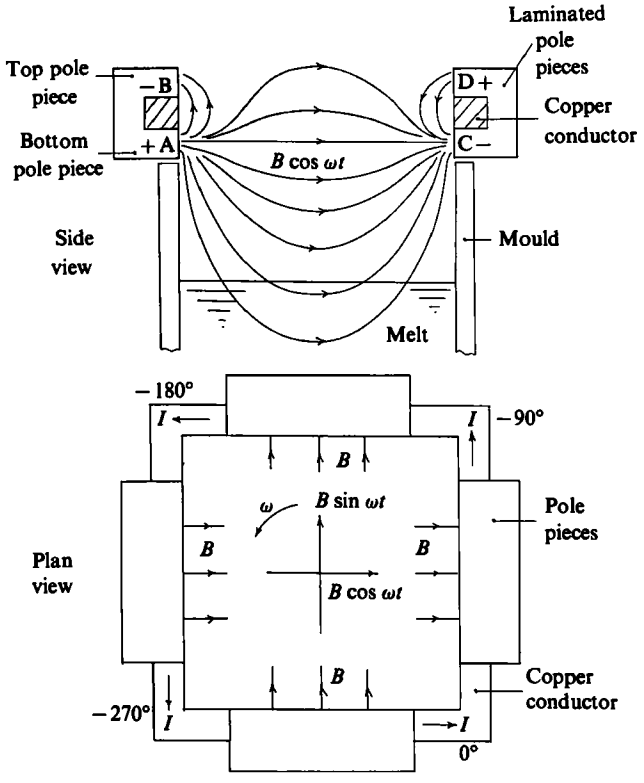

FIGURE 11. Idealized view of stirrer.

strength weaker than that of the bottom pole pieces, since there is no flux linkage between D and B. The ratio of the top-pole-piece strength to the bottom-pole-piece strength is chosen such that B and D are at the same potential. The bottom-pole-piece strength is given by Ampère's law

$$\int_A^B \boldsymbol{B}\cdot \mathrm{d}\boldsymbol{r} = \mu I \quad (I = \text{copper bar current}).$$

The resulting magnetic field is shown in figure 12. In §12 we shall compare this simple two-dimensional field with measurements of the magnetic field generated by the experimental stirrer. Somewhat fortuitously, it turns out that this simple model gives a reasonable approximation of the real field, except in the region of the pole pieces. However, we shall use the measured values of magnetic-flux density, rather than this model, to calculate the body force.

11. The nature of the body force generated by the magnetic field in the experiments

Consider any irrotational two-dimensional field. For convenience, let this field lie in the (x, y)-plane

$$\boldsymbol{B}_0 = B_x(x,y)\,\boldsymbol{i} + B_y(x,y)\boldsymbol{j} = \nabla \times (-\psi \mathbf{k}).$$

The current density is

$$\boldsymbol{J} = \sigma \frac{\partial \psi}{\partial t}\boldsymbol{k},$$

and the body force is given by

$$\boldsymbol{F} = \boldsymbol{J} \times \boldsymbol{B} = -\sigma \frac{\partial \psi}{\partial t} \nabla \psi.$$

If ψ is sinusoidal, $\psi = \hat{\psi} \sin(\omega t)$, then

$$\boldsymbol{F} = -\tfrac{1}{4}\omega\sigma \nabla(\hat{\psi}^2) \sin(2\omega t).$$

This force is conservative and consequently it is unable to produce any fluid motion. (The result does not hold if $\boldsymbol{B}$ is rotational.) This is an important result with regard to the stirrer used here. If we are looking for the rotational body force resulting from two, low-frequency, perpendicular, phased, two-dimensional fields, then we must take the cross-product of the current density generated by one field with the other field, and vice versa. A current reacted against its own field will produce only a conservative body force.

In the TIRL stirrer we have two-dimensional fields in two mutually perpendicular vertical planes. Each of these produce currents in a horizontal plane. The rotational part of the body force arises from reacting these horizontal currents against the vertical components of the complementary fields. The resulting force lies in a horizontal plane and will tend to rotate the fluid in the same direction as the field.

The magnetic field and current density in a TIRL stirrer may be expressed in the following form (where z is along the axis of the column)

$$\boldsymbol{B} = \boldsymbol{B}_1(x, z) \cos(\omega t) + \boldsymbol{B}_2(y, z) \sin(\omega t),$$

where

$$\boldsymbol{B}_1 = (B_{1x}, 0, B_{1z}),$$

$$\boldsymbol{B}_2 = (0, B_{2y}, B_{2z}),$$

and

$$\boldsymbol{J} = \boldsymbol{J}_1(x, z) \sin(\omega t) + \boldsymbol{J}_2(y, z) \cos(\omega t),$$

where

$$\boldsymbol{J}_1 = (0, J_{1y}, 0),$$

$$\boldsymbol{J}_2 = (J_{2x}, 0, 0).$$

The rotational part of the body force is given by

$$\boldsymbol{F} = \boldsymbol{J}_1 \times \boldsymbol{B}_2 \sin^2(\omega t) + \boldsymbol{J}_2 \times \boldsymbol{B}_1 \cos^2(\omega t).$$

Extracting the steady part of this force, we obtain

$$\boldsymbol{F} = \tfrac{1}{2}(J_{1y} B_{2z}, -J_{2x} B_{1z}, 0).$$

Note that there is no axial component of force.

We now expand the components of $\boldsymbol{B}$ and $\boldsymbol{J}$ as Taylor series about the z-axis. To first order in x/R and y/R, the current density is constant in x and y, while the vertical components of magnetic field vary linearly with distance from the axis.

$$\left.\begin{aligned} J_{1y} &\approx \sigma\omega BRg\left(\frac{z}{R}\right) \\ J_{2x} &\approx \sigma\omega BRg\left(\frac{z}{R}\right) \\ B_{1z} &\approx -Bh\left(\frac{z}{R}\right)\frac{x}{R} \\ B_{2z} &\approx -Bh\left(\frac{z}{R}\right)\frac{y}{R} \end{aligned}\right\} \quad \text{to first order in } \frac{x}{R} \text{ and } \frac{y}{R},$$

where $g(z/r)$ and $h(z/R)$ are dimensionless functions and B is a characteristic field strength. It may be shown that if $h(z/R) > 0$, then $g(z/R) > 0$.

Substituting these expressions into the equation for the steady part of the rotational body force, we deduce

$$\boldsymbol{F} = \tfrac{1}{2}\sigma\omega B^2 g\left(\frac{z}{R}\right) h\left(\frac{z}{R}\right)(-y, x, 0).$$

If we let $f(z/R) = g(z/R)\, h(z/R)$, and change from a Cartesian to a cylindrical polar coordinate system, then this expression for the body force becomes

$$\boldsymbol{F} = \tfrac{1}{2}B^2\sigma\omega r f\left(\frac{z}{R}\right)\hat{\boldsymbol{e}}_\theta,$$

which is the same as equation (1), and is the idealized force distribution used in the analysis of §§3–8.

This expression is only valid near the z-axis. In general, we would expect higher-order terms in r/R to be significant for larger values of r. Magnetic field measurements made in the stirrer, and inferred eddy current distributions, show that the products $J_{2x}B_{1z}$ and $J_{1y}B_{2z}$ are approximately linear in x and y, to within 20%, throughout the range $0 < r < 0.8R$. However, they are significantly lower than the linear variation would imply in the range $0.8R < r < R$. It is estimated, from measured values of $\boldsymbol{B}$, that an assumed linear variation of F_θ in r will lead to an overestimate of the net applied magnetic torque of about 60%.

None the less, in order to compare the measured velocities with the theoretical analysis, we must make the approximation that F_θ is linear in r. We shall follow this route, while remembering that this approximation is relatively poor and will lead to a significant overestimate of the net applied torque. (Note also that nonlinear variations of $J_{2x}B_{1z}$ and $J_{1y}B_{2z}$ with x and y lead to a non-axisymmetric body force and a radial component of force.)

12. Experimental results

12.1. *Magnetic-field measurements and calculation of the body force*

The magnetic field was measured at 1 cm intervals throughout the cylinder.

It was suggested in §2 that the applied magnetic field in the mercury may be considered fully diffused, and that a low-frequency approach to the problem should be a good approximation. The simplest way of testing this assumption is to measure the magnetic field in the cylinder, with and without mercury present.

The horizontal component of the centreline magnetic field, for both an empty and full tube, is shown in figure 13. It is clear that, within the first skin depth of the mercury, attenuation of the magnetic field by eddy currents is negligible. Beyond that point, the field is so small that it does not matter whether diffusion is dominant or not.

It is proposed in §10 that the applied magnetic field can be approximated by two, two-dimensional fields, oscillating 90° out of phase and mutually perpendicular

$$\boldsymbol{B} = \boldsymbol{B}_1(x, z)\cos(\omega t) + \boldsymbol{B}_2(y, z)\sin(\omega t),$$

where

$$\boldsymbol{B}_1 = (B_{1x}, 0, B_{1z}),$$

$$\boldsymbol{B}_2 = (0, B_{2y}, B_{2z}).$$

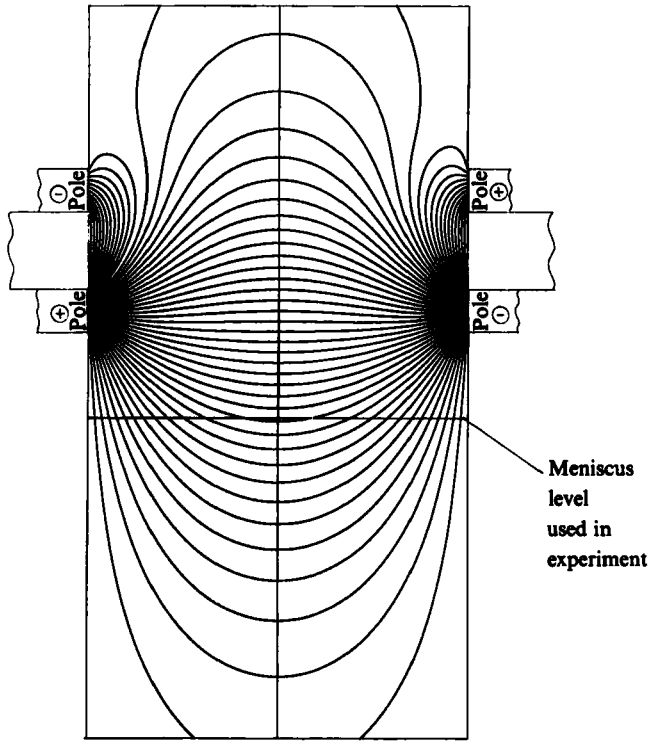

FIGURE 12. Complex potential plot of two-dimensional field.

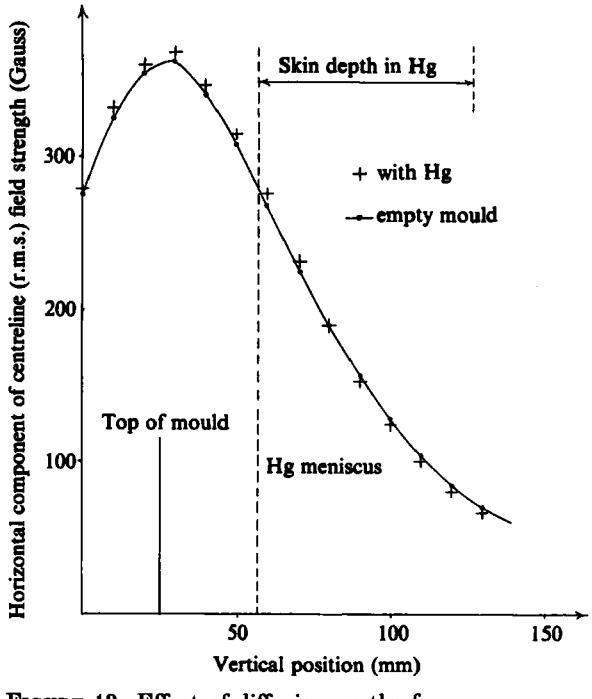

FIGURE 13. Effect of diffusion on the free space magnetic field.

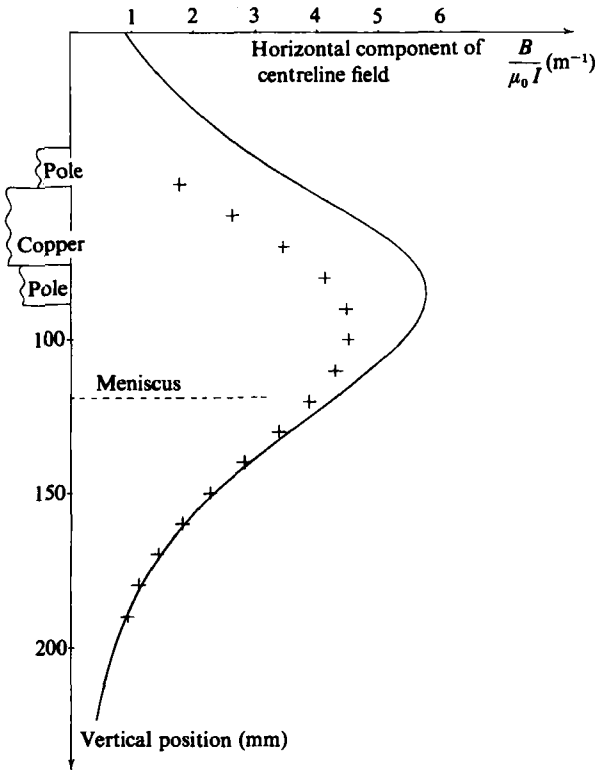

FIGURE 14. Comparison of predicted and measured magnetic flux densities. —, two-dimensional theory; +, measured.

Analysis of the measured magnetic field data shows that B_x is sensibly independent of y across the width of the pole pieces, and that B_y is independent of x in the same range. The data also shows that B_x and B_y are symmetric in both x and y. This supports the notion that the field may be approximated by two, two-dimensional fields.

In §10, a simple potential is proposed for $\boldsymbol{B}_1(x,z)$ (or $\boldsymbol{B}_2(y,z)$) which is based on the complex potential for distributed sinks and sources. This theoretical field is shown in figure 12. In figure 14, the centreline field strength predicted by the complex potential model is compared with the equivalent measured field. While there is some divergence between the theoretical and measured fields near the pole pieces, the agreement is to within 10% below the pole pieces and in the liquid.

In order to interpret the velocity measurements it is necessary to determine the body-force distribution in the fluid. There are two possible approaches to this. One method is to use the two-dimensional, complex potential model of the magnetic field, in conjunction with the theory outlined previously. A preferable approach, however, is to use the magnetic field measurements, since this assumes less about the distribution of $\boldsymbol{B}$.

To evaluate F_θ from the magnetic field data, we have taken advantage of the approximate biplanar distribution of $\boldsymbol{B}$, and used the corresponding theory outlined in §11. Inevitably, the assumption that $\boldsymbol{B}$ comprises two, two-dimensional fields, will lead to some errors in determining $\boldsymbol{J}\times\boldsymbol{B}$. However, since we have already made the

severe approximation that F_θ is linear in r, these errors should be relatively acceptable.

In order to evaluate F_θ, we must first determine the vector potential $\boldsymbol{A}$ corresponding to the measured values of $\boldsymbol{B}$. Faraday's equation then gives $\mathbf{J}$, and the time-averaged body force follows from

$$\boldsymbol{F} = \tfrac{1}{2}(J_{1y} B_{2z}, -J_{2x} B_{1z}, 0).$$

Note that Ampère's law cannot be used to determine $\boldsymbol{J}$ since $\nabla \times \boldsymbol{B} = \mathbf{0}$, to first order in Δ.

For a two-dimensional field, $\boldsymbol{A}$ is given by the magnetic streamfunction ψ. This streamfunction can be determined from measured values of the magnetic field by application of the appropriate finite-difference formulae. However, it is desirable to relax the magnetic field data before calculating ψ. There are two reasons for doing this. Firstly, the data should be smoothed in some way before applying the finite-difference approximations. Secondly, it is only possible to introduce ψ if the field is truly two-dimensional. In practice the magnetic field has a tendency to three-dimensional behaviour.

Measurements of $B_x(x, z)$ on a vertical cross-section of the tube were analysed. If $\boldsymbol{B}_1$ were exactly two-dimensional, and there were no errors in the measurements, then B_x should satisfy

$$\frac{\partial^2 B_x}{\partial x^2} + \frac{\partial^2 B_x}{\partial z^2} = 0.$$

Inevitably, the magnetic field data did not exactly satisfy this. Consequently, a relaxation procedure was applied to the measurements, whereby the residuals (in calculating $\nabla^2 B_x$) were reduced. This changed the original data by, on average, 6%.

The magnetic streamfunction $\psi(x, z)$, vertical field component $B_z(x, z)$, and potential $\phi(x, z)$ were then determined from $B_x(x, z)$ by application of the appropriate finite-difference formulae to

$$B_x = -\frac{\partial \phi}{\partial x} = -\frac{\partial \psi}{\partial z},$$

$$B_z = -\frac{\partial \phi}{\partial z} = +\frac{\partial \psi}{\partial x}.$$

The shape of the resulting field is shown in figure 15. This bears a reasonable resemblance to the shape of the potential field predicted in §10, except in the vicinity of the pole pieces. Note that we would not expect the processed experimental data to be accurate in the vicinity of the pole pieces. The high field gradients in those regions make extrapolations from measurements 1 cm apart very unreliable.

In §11, it was shown that, to first order in r/R, the magnetic force distribution is given by

$$F_\theta = [\tfrac{1}{2} B_0^2 \sigma \omega r] f(z),$$

where B_0 is a reference field strength.

Following the procedure outlined in §11, the depth function $f(z)$ has been calculated from the relaxed magnetic field data. This is shown in figure 16. It can be seen that the force decays rapidly with depth. (Note that, since $f(z)$ is multiplied by σ to obtain F_θ, the body force above the meniscus is zero, although $f(z)$ is shown as non-zero.)

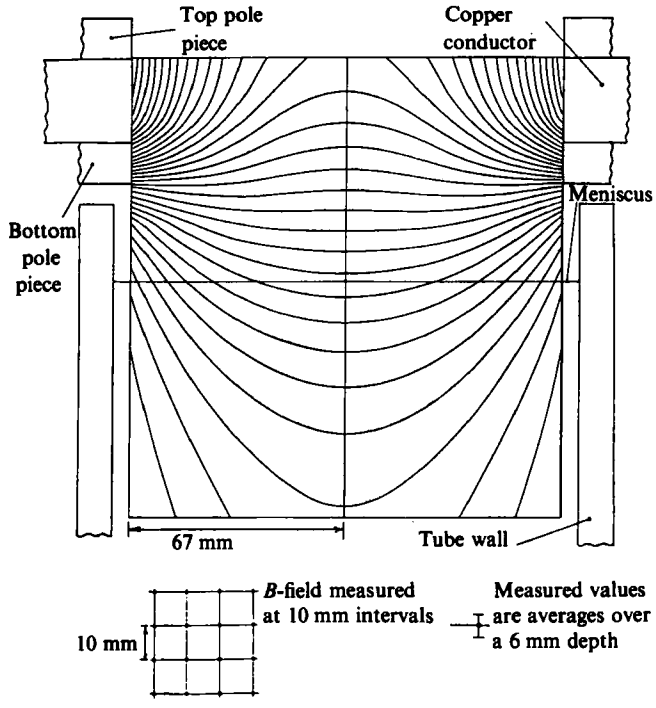

FIGURE 15. Measured magnetic field in a vertical plane of the cylinder.

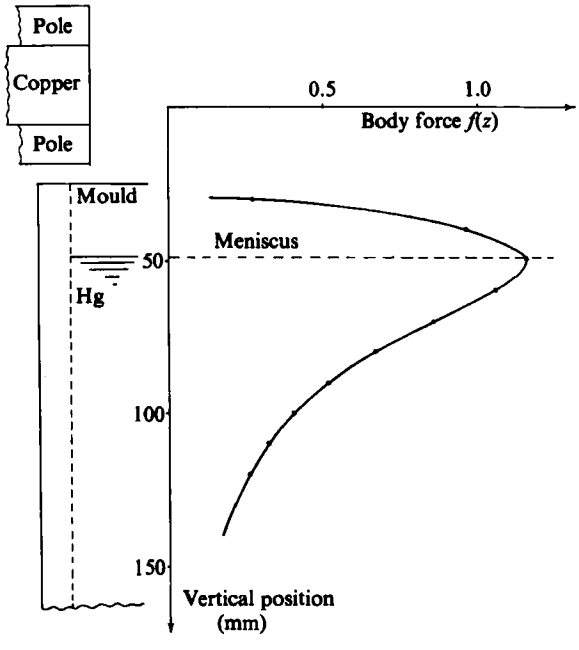

FIGURE 16. Variation of body force with depth.

The reference point for B_0 was chosen to be on the cylinder centreline, 8 mm below the meniscus. The magnitude of B_0 depends on the stirrer power. A range of stirrer powers was available in the experiment corresponding to different transformer supply voltages. For maximum power, at which most of the following velocity measurements were taken, $B_0 = 0.0317\,T$. The corresponding characteristic velocity is $\bar{V} = 0.359$ m/s.

12.2. *Velocity measurements*

The signal from the velocity drag probe shows that the flow is turbulent, with the typical fluctuating component of velocity being approximately 2% of the mean velocity. The turbulence lies predominantly in the low-frequency range $0.5 \rightarrow 7$ Hz.

In this investigation we are not concerned with the details of the turbulence, but merely with mean flow measurements. For most measurements, therefore, the drag-probe signal was put through a low-pass filter, which suppresses frequencies above $\frac{1}{2}$ Hz. However, it was found that the mean flow velocity fluctuated by up to $\pm 10\%$ with a period of between a few seconds and one minute. This was due to precessing of the vortex core, a characteristic feature of swirling flows (see Gupta *et al.* 1984). In taking mean flow measurements, these fluctuations were averaged out over a period of time. However, they still caused some problem in obtaining repeatable results.

Using the rotating vane, the variation of average surface angular velocity with applied field strength was measured. This is shown in figure 17. It is clear that the measured velocity scales linearly on $\bar{V}$. The results discussed below were taken at maximum stirrer power, corresponding to $\bar{V} = 0.359$ m/s.

Velocity profiles for $u_\theta(r)$ were measured in the forced region of the flow ($z \leqslant 13$ cm) using the drag probe. Figures 18 and 19 give the radial profiles of u_θ at $z = 2.8$ cm and $z = 7.8$ cm. In this region of the flow, the theory indicates that there is a balance of electromagnetic and inertial forces. The theoretical curves shown in these figures are derived from this balance and so are independent of any model for turbulent shear stresses. These theoretical curves are obtained by substituting the appropriate values of force integral p, found by integrating figure 16, into equations (27)–(31). The mean core rotation rates, measured using the rotating vane, are also shown

The two experimental measurements are consistent with each other, to within the accuracy of the instruments. They also agree with the theoretical curve at $z = 2.8$ cm over the central part of the cross-section. But the theory significantly overestimates the velocity in the outer part of the flow, particularly at $z = 7.8$ cm. The discrepancy is as large as 75% near the wall. The reasons for the difference between the theoretical and experimental curves are probably,

(i) the assumed linear dependence of F_θ on r, used in the theory, leads to an overestimate of the net applied magnetic torque of about 60%. This overestimate will manifest itself in the theoretical curves;

(ii) the theoretical analysis does not allow for the effects of turbulent shear in the forced region. This shear will tend to lower the velocity, particularly near the wall, from the value predicted by inviscid analysis.

The velocity profile in figure 19 appears not to pass through the origin, and this must raise questions regarding the validity of measurements made near the z-axis. The discrepancy probably arises from a combination of precessing of the vortex core and the intrusive nature of the drag probe. These features may also account for the difference between the rotating vane and drag-probe measurements.

In figure 20 the measured angular velocity is shown as a function of depth. Curves are given for three different radii, $r = 2$, 3 and 4 cm. To avoid confusion, some error

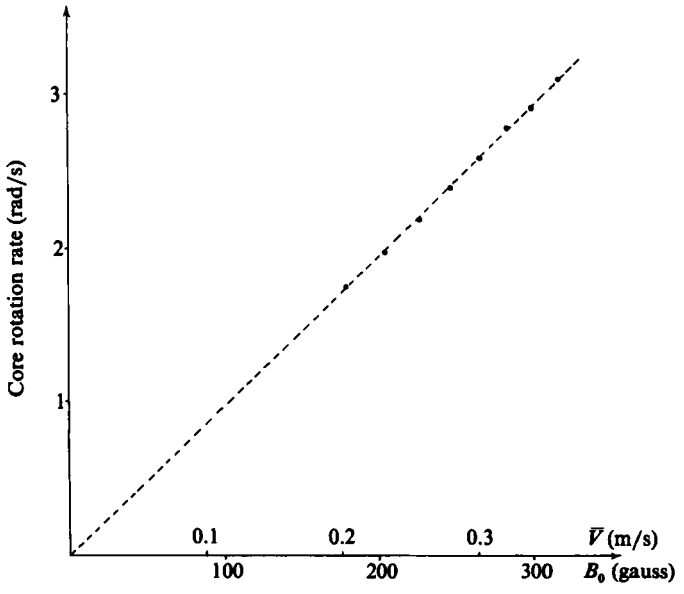

FIGURE 17. Variation of surface core angular velocity with B_0. (Measured using rotating vane.)

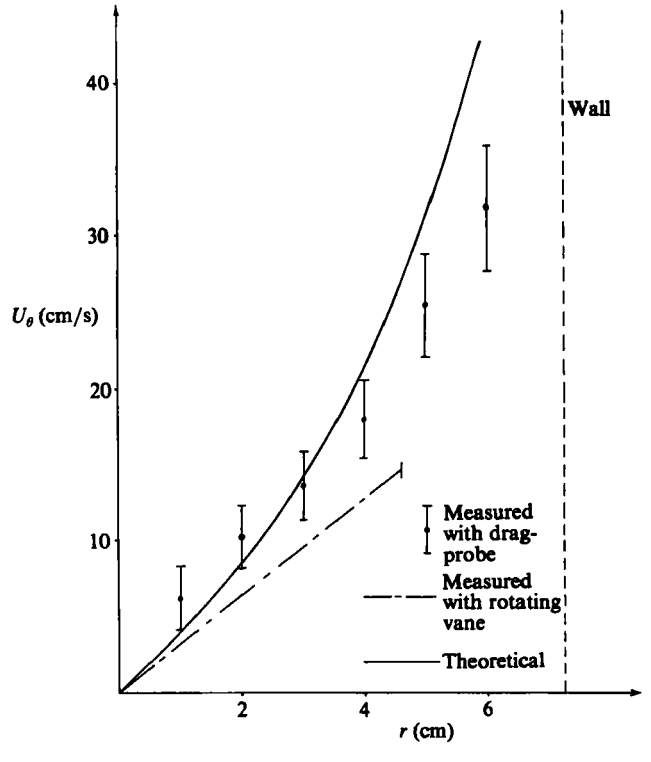

FIGURE 18. Comparison of measured and theoretical velocities (2.8 cm below surface).

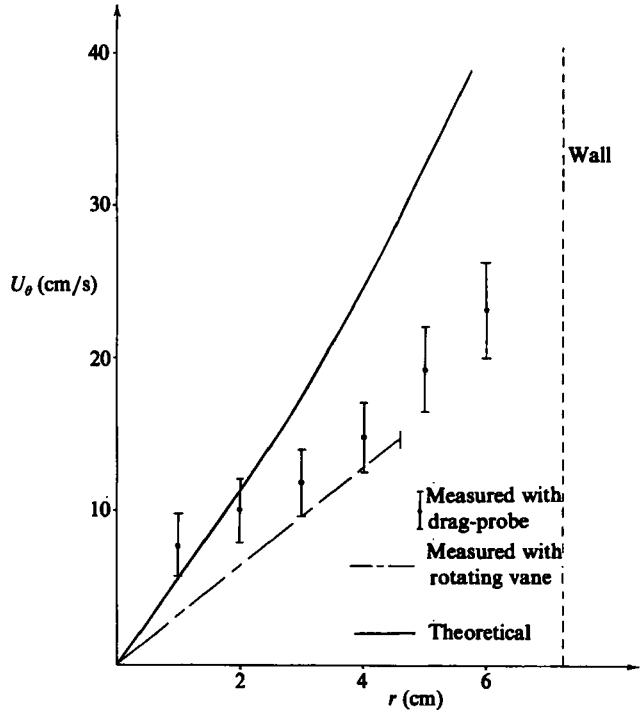

FIGURE 19. Comparison of measured and theoretical velocities (7.8 cm below surface).

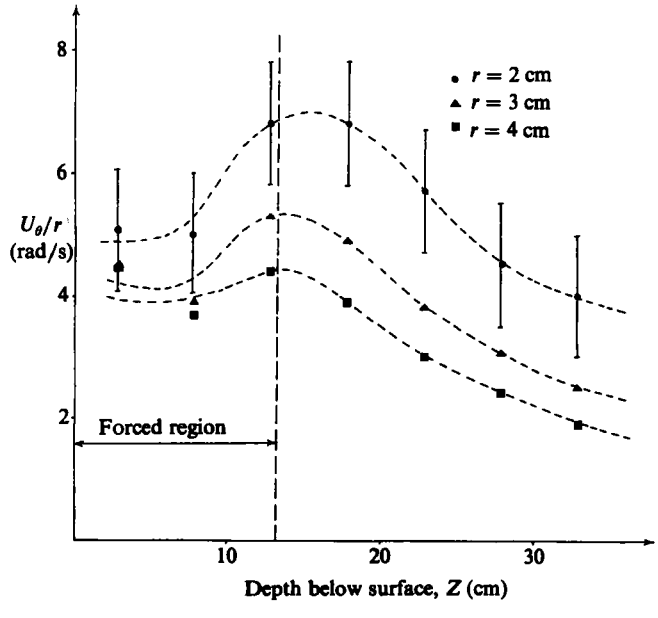

FIGURE 20. Variation of angular velocity with depth.

bars have been omitted from the data points. These error bars are sufficiently large for it to be difficult to determine the true shape of the profiles $u_\theta(z)$. None the less, there are two discernible trends in the data. Firstly, the swirl extends well out of the forced region, the lengthscale for the axial decay of swirl being of the order of $15R$. This is consistent with the theoretical discussion given in §4, in which the axial lengthscale in the unforced region is predicted as $L = \mathbb{R}_t R$.

The second trend which is evident in figure 20 is that there is a maximum in u_θ/r near the bottom of the forced region. This is also consistent with the theoretical arguments presented in §6 and Appendix A, and indicates that inertia is dominant over shear in balancing the body force.

13. Conclusions

We have shown that an important distinction between one-dimensional (swirl only) and two-dimensional (swirling recirculating) flows is that in the former, since there is no secondary flow, the magnetic torque is balanced by shear. When there is recirculation, the body force is locally balanced by a flux of angular momentum out of the forced region.

In one-dimensional flow the magnitude and distribution of the swirl is very different depending on whether the flow is laminar or turbulent. This reflects the different nature of viscous and Reynolds stresses. The turbulent case may be adequately modelled using a simple 'mixing-length' representation for the Reynolds stresses.

When there is recirculation, order-of-magnitude analysis and computations show that the secondary flow is as large as the primary swirl flow. This secondary flow, which results from differential rotation, sweeps the angular momentum into the unforced region so that the forced vortex ultimately penetrates some distance beyond the driven region. The axial lengthscale of the recirculating eddy is controlled by wall shear and is sufficient to ensure that the applied magnetic torque is balanced by shear on the sidewalls. As the wall friction is increased, the degree of penetration of swirl is decreased, although its maximum magnitude remains unaltered. This maximum occurs just at the level where the body force drops to zero, showing that it is the history of forcing of fluid elements that determines the swirl, not the local value of the body force.

An approximate solution to the inviscid equations of motion is proposed for the forced region in which the overall angular momentum budget is satisfied. This solution incorporates the empirical observation that u_θ is linear in r in the overlap region. A comparison of this approximate analytical solution with numerical experiments gives satisfactory results.

Many of the broad trends predicted by the analysis have been reproduced experimentally. Measured values of swirl are shown to scale on $\bar{V} = \{B(\sigma/\rho\omega)^{\frac{1}{2}}\}\omega R$, and to have a maximum at the bottom of the forced region. In addition, the swirl extends well out of the driven region and decays slowly with depth, with an axial lengthscale compatible with the theoretical estimate of $L \sim \mathbb{R}_t R \sim 30R$.

On comparing measured values of swirl with that predicted by the theory, the inviscid analysis tends to overestimate the observed velocity. The difference is most marked near the wall where the theory overestimates the swirl by as much as 75%. Part of this discrepancy is due to the fact that the theoretical analysis assumes implicitly that F_θ varies linearly with r, which leads to an overestimate of the total applied magnetic torque of 60%. In addition, the theory does not allow for the effects

of shear in the forced region. This shear will reduce the velocity, particularly near the wall, to a value below that predicted by the inviscid analysis. Despite these discrepancies, the measured velocity field is broadly in line with that predicted by the theory.

The authors wish to thank T.I. Research Laboratories for their support in this study and also Dr F. Boyson for his assistance in the numerical computations. The computer code used was a modified version of FLUENT made available by Creare R & D.

Appendix A. Variation of swirl with depth in the forced region

We shall show that, in the forced region, u_θ increases with depth near the axis and near the wall ($r = R$).

The governing equations are

$$\boldsymbol{u}\cdot\nabla\Gamma = \tfrac{1}{2}\bar{V}^2\left[\frac{r}{R}\right]^2 f\left(\frac{z}{R}\right),$$

$$\boldsymbol{u}\cdot\nabla\left[\frac{\omega_\theta}{r}\right] = \frac{\partial}{\partial z}\left(\frac{\Gamma^2}{r^4}\right).$$

The first equation shows that the angular momentum must increase along a streamline. Near the wall we have

$$u_z\frac{\partial\Gamma}{\partial z} = \tfrac{1}{2}\bar{V}^2 f\left(\frac{z}{R}\right),$$

from which we deduce $\partial u_\theta/\partial z > 0$ on $r = R$.

Near the axis, however, the situation is less clear. In the vicinity of the axis we have a forced vortex, $\Gamma \approx \Omega(z)\,r^2$, and $u_z \approx u_0(z)$, where $u_0(z)$ is negative. Substituting these expressions for u_z and Γ into the transport equation for Γ (u_r may be derived from $\nabla\cdot\boldsymbol{u} = 0$), and letting r tend to zero, we deduce

$$u_0\,\Omega'(z) - \Omega u_0'(z) = \frac{1}{2}\left[\frac{\bar{V}}{R}\right]^2 f\left(\frac{z}{R}\right).$$

This equation shows that there are two ways in which we may guarantee that Γ increases along a streamline. Either Ω increases as the fluid particle moves towards the surface, or the streamline turns radially outwards into a region of higher swirl. It is not possible to tell from the angular momentum equation which of these two mechanisms is dominant. We must turn to the equation for azimuthal vorticity.

We know that ω_θ/r is negative at the bottom of the forced region on the axis, increasing to zero at the surface. This suggests that ω_θ/r increases along a streamline near the axis, and it follows from the transport equation for ω_θ/r that $\Omega'(z) > 0$.

We have shown, therefore, that u_θ is an increasing function of depth in the forced region, both near the axis and near the wall. This result is somewhat surprising. It contrasts with the situation where shear, rather than inertia, is dominant, in which case we would expect u_θ to decay with depth.

Appendix B. Asymptotic matching of the forced and unforced regions

Here we consider how the forced and diffusive regions match each other as $F_\theta \to 0$ and the boundary layer grows. We shall show that, in the overlap region, the flow is essentially unforced and inviscid, and that axial gradients are zero to first order in $\mathbb{R}^{-1}$. It is convenient to rewrite the transport equations (14) and (15) in dimensionless form. Following the scaling laws established in §4, we introduce the following dimensionless forms of the variables,

$$\hat{\Gamma} = \frac{\Gamma}{\bar{V}R},$$

$$\hat{\psi} = \frac{\psi}{\bar{V}R^2},$$

$$\epsilon = \frac{\nu}{\bar{V}R} = \mathbb{R}^{-1},$$

$$\hat{s} = \frac{s}{R^2},$$

$$x = \frac{z}{\mathbb{R} \times R} \quad \text{(outer variable)},$$

$$X = \frac{z}{R} = \frac{x}{\epsilon} \quad \text{(inner variable)}.$$

For clarity, the hats on $\hat{\Gamma}$, $\hat{\psi}$ and $\hat{s}$ will be omitted in the following analysis.

The overlap region shown in figure 5 exists when we simultaneously take the limits $X \to \infty$, $x \to 0$.

Let
$$\psi = \psi^{[0]} + \epsilon\psi^{[1]} + \epsilon^2\psi^{[2]} + \ldots,$$
$$\Gamma = \Gamma^{[0]} + \epsilon\Gamma^{[1]} + \epsilon^2\Gamma^{[2]} + \ldots.$$

These expansions may be substituted into the transport equations and coefficients of ϵ^n equated to zero. The resulting zero-order equations in the forced region are,

$$\left\{-\frac{\partial\psi^{[0]}}{\partial X}\frac{\partial}{\partial s} + \frac{\partial\psi^{[0]}}{\partial s}\frac{\partial}{\partial X}\right\}\Gamma^{[0]} = \tfrac{1}{4}sf(X),$$

$$\left\{-\frac{\partial\psi^{[0]}}{\partial X}\frac{\partial}{\partial s} + \frac{\partial\psi^{[0]}}{\partial s}\frac{\partial}{\partial X}\right\}\left[\frac{\partial^2\psi^{[0]}}{\partial s^2}\right] = -\frac{1}{8s^2}\frac{\partial(\Gamma^{[0]})^2}{\partial X}.$$

These are, of course, the inviscid equations of motion. In the diffusive region the appropriate axial variable is x. If we assume that for large X the dimensionless force function $f(X)$ is of the form $X^{-n}(n \geqslant 2)$, then to zero order in ϵ, the forcing term drops out of the transport equations in the diffusive region. The resulting zero-order equations are

$$\left\{-\frac{\partial\psi^{[0]}}{\partial x}\frac{\partial}{\partial s} + \frac{\partial\psi^{[0]}}{\partial s}\frac{\partial}{\partial x}\right\}\Gamma^{[0]} = 2s\frac{\partial^2\Gamma^{[0]}}{\partial s^2}, \tag{B 1}$$

$$\left\{-\frac{\partial\psi^{[0]}}{\partial x}\frac{\partial}{\partial s} + \frac{\partial\psi^{[0]}}{\partial s}\frac{\partial}{\partial x}\right\}\left[\frac{\partial^2\psi^{[0]}}{\partial s^2}\right] = \frac{2}{s}\frac{\partial}{\partial s}\left(s^2\frac{\partial^3\psi^{[0]}}{\partial s^3}\right) - \frac{1}{8s^2}\frac{\partial(\Gamma^{[0]})^2}{\partial x}. \tag{B 2}$$

We now consider the overlap region where $x \to 0$ and $X \to \infty$. We expect that this region is, to zero order, both unforced and inviscid.

Let

$$q = X\epsilon^{\alpha}, \quad 0 < \alpha < 1.$$

Rewriting the transport equations in terms of q and taking the limit $\epsilon \to 0$, with q fixed, we obtain

$$\left\{-\frac{\partial \psi}{\partial q}\frac{\partial}{\partial s}+\frac{\partial \psi}{\partial s}\frac{\partial}{\partial q}\right\}\Gamma = 0, \tag{B 3}$$

$$\left\{-\frac{\partial \psi}{\partial q}\frac{\partial}{\partial s}+\frac{\partial \psi}{\partial s}\frac{\partial}{\partial q}\right\}\left(\frac{\partial^2 \psi}{\partial s^2}\right) = -\frac{1}{8s^2}\frac{\partial \Gamma^2}{\partial q}. \tag{B 4}$$

These equations represent unforced inviscid flow. They are appropriate to the overlap region since if $\epsilon \to 0$, with q fixed, then $X \to \infty$ and $x \to 0$.

It is instructive to match gradients in the overlap region.

$$\operatorname*{Lim}_{X\to\infty}\frac{\partial \Gamma}{\partial X} = \operatorname*{Lim}_{x\to 0}\epsilon\frac{\partial \Gamma}{\partial x},$$

from which

$$\operatorname*{Lim}_{X\to\infty}\frac{\partial \Gamma^{[0]}}{\partial X} = 0. \tag{B 5}$$

Similarly,

$$\operatorname*{Lim}_{X\to\infty}\frac{\partial \psi^{[0]}}{\partial X} = 0. \tag{B 6}$$

In order to accommodate the change in axial lengthscale, axial derivatives of $\Gamma^{[0]}$ and $\psi^{[0]}$ are zero in the overlap region. This is shown in figure 5. Note that conditions (B 5) and (B 6) are sufficient to satisfy the transport equations (B 3) and (B 4) in the overlap region.

REFERENCES

Batchelor, G. K. 1951 Note on a class of solutions of the Navier–Stokes equations representing steady rotationally-symmetric flow. *Q. J. Mech. Appl. Maths* **4**, 29–41.

Batchelor, G. K. 1956 On steady laminar flow with closed streamlines at large Reynolds number. *J. Fluid Mech.* **1**, 177–190.

Dahlberg, E. 1972 On the action of a rotating magnetic field on a conducting liquid. *AB Atomenergi Rep.* AE-447. Sweden.

Davidson, P. A. 1985 Estimation of turbulence velocities induced by magnetic stirring during continuous casting. *Mat. Sci. Tech.* **1**, 994–999.

Davidson, P. A. 1986 MHD of swirling, recirculating flow. PhD thesis, University of Cambridge.

Davidson, P. A. & Boyson, F. 1987 The importance of secondary flow in the rotary electromagnetic stirring of steel during continuous casting. *Appl. Sci. Res.* vol. 44.

Greenspan, H. P. 1968 *The Theory of Rotating Fluids.* Cambridge University Press.

Gupta, A. K., Lilley, D. G. & Syred, N. 1984 *Swirl Flows.* Energy and Engineering Science Series. Abacus.

Lamb, H. 1959 *Hydrodynamics.* 6th edn. Cambridge University Press.

Moffatt, H. K. 1978 Rotation of liquid metal under the action of a rotating magnetic field. In Branover, H. & Yakhot, A. (eds.) MHD – Flows and Turbulence II. Israel University Press, 45–62.

Moore, D. J. 1982 Magnetohydrodynamics of the coreless induction furnace. PhD thesis, University of Cambridge.

Patankar, S. V. 1980 *Numerical Heat Transfer and Fluid Flow.* Hemisphere.

ROBINSON, T. 1973 An experimental investigation of a magnetically driven rotating liquid-metal flow. *J. Fluid Mech.* **60**, 641–664. (With an Appendix by K. Larsson.)

RODI, W. 1984 Turbulence models and their applications in hydraulics. State-of-the-art paper. IAHR.

TACKE, K. H. & SCHWERDTFEGER, K. 1979 Stirring velocities in continuously cast round billets as induced by rotating electromagnetic fields. *Stahl und Eisen* **99**, 7–12.